Diese Arbeit wurde vorgelegt am Physikalischen Institut III A

Setup of an optical system for autonomous surveillance of orbital objects

von

Pascal Mösbauer

Masterarbeit in Physik

vorgelegt der

Fakultät für Mathematik, Informatik und Naturwissenschaften
der RWTH Aachen

im Mai 2018

angefertigt im

III. Phys. Institut, RWTH Aachen

bei

Prof. Dr. Thomas Hebbeker
PD. Dr. Oliver Pooth

Abstract

As space becomes more and more crowded, the probability of collisions between space debris and active satellites or manned space missions increases. Active space debris removal missions are being planned to remove the most dangerous objects from earth orbit, however the planning of such missions requires many properties of the target object to be known.
Ground-based observations might be able to yield these properties. In this work, a simple mobile observation system is assembled and programmed to perform passive optical tracking. The final configuration of the system is capable of performing measurements, tracking and creating light curves.
It becomes clear that the tracking accuracy of the mobile system is limited primarily by the pointing precision. Influences seen in the light curves such as the additional atmospheric attenuation for larger zenith angles can be eliminated if necessary by calibrations, although it is unclear whether the obtained light curves can be used for fingerprinting. The capabilities of the system are proved by evaluating the rotation period of Cosmos-2375.
Through the use of a CMOS sensor with Bayer filter, the reflected signal of the observation target can be measured at three different wavelengths. Although no reliable results could be drawn from the multispectral observations in this thesis, the recurring signal peak that is solely visible in the red color channel of the observation of Cosmos-2375 warrant further investigation. An inexpensive, simple system such as the presented one may increase the accuracy of future space debris observations.

Special thanks go out to Thomas Hasenohr and Dr. Daniel Hampf who made this thesis possible and supervised me. I am deeply grateful for the offered help and feedback provided by Ewan Schafer, Niklas Eicker and Oliver Curkovic. But above all, I would like to thank everyone whom I got to know at the institute for making the many hours of work in the last year a pleasant and interesting time.

In Gedenken an meine Mutter, ohne die ich es niemals bis hier geschafft hätte. Ich bewundere dein Durchhaltevermögen mit jedem Tag mehr und du wärst stolz, wenn du uns jetzt sehen könntest. Danke für alles.

Contents

List of abbreviations

ASA	Astrosysteme Austria
CR2	canon raw image
DLR	German Aerospace Center
FOV	field of view
ISS	international space station
LCM2	LightCurveMaker2
LEO	low earth orbit
MS-DOS	Mobile Satellite and Debris Observation System
MEO	middle earth orbit
OOOS	Orbital Objects Observation Software
ROI	region of interest
SLR	satellite laser ranging
TLE	Two Line Element
UFO	Uhlandshöhe Forschungsobservatorium
h	hour angle position of an object
δ	declination position of an object

1. Introduction

Since the middle of the last century, humanity has been interested in the use of space. The launch of Sputnik 1, the first man-made earth satellite, initiated the era of spaceflight on October 4, 1957. The development of new satellite technologies was fueled by the political tensions of the time. During the 80s and 90s, sometimes more than hundred rocket launches per year brought new satellites into space.[1]
Over sixty years of space utilization, objects such as used upper and transfer stages, dead satellites and slag particles from solid rocket propulsion systems have accumulated in all orbits around the globe.[2, p. 16 ff.] SATCAT is a catalog of launched payloads and debris objects that listed a total of 18,808 man-made objects in Earth orbits in November, 2017. All these objects move with hypervelocity and only 1,916 of them are active.[3]
As the number of objects in orbit increases, so too does the probability of collisions occurring between two objects. With increasing frequency, satellite operators are required to perform debris avoidance maneuvers. One of the most prominent incidents was the collision of Iridium 33 with the inoperative satellite Cosmos-2251 on February 10, 2009. The collision produced almost 2,000 fragments whose contribution can be seen in Fig. 1.1.[4]

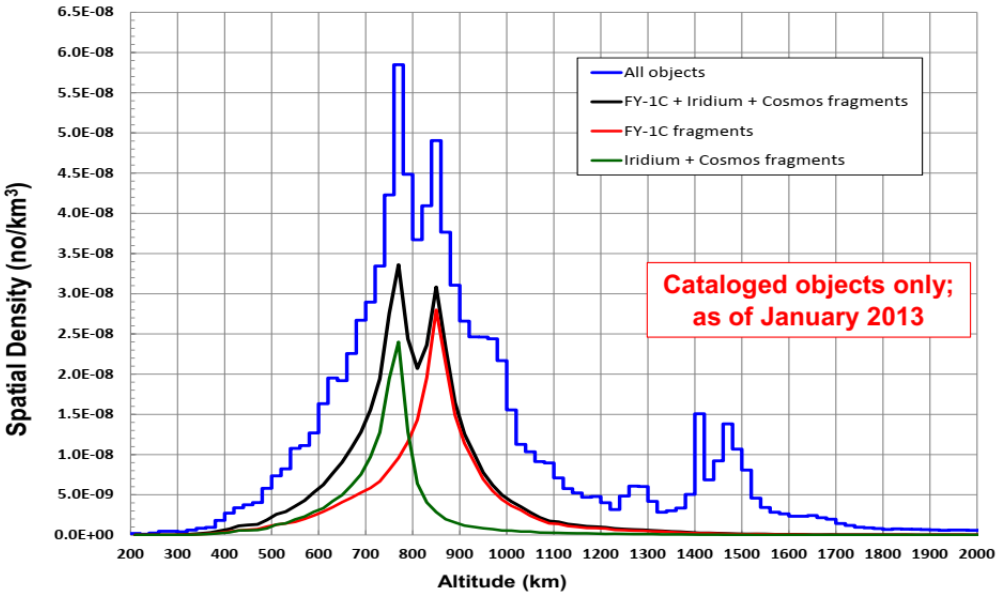

Figure 1.1.: Concentration of cataloged objects in LEO.[2, p. 15]

All orbital objects of more than a few centimeters in diameter pose a threat to other active satellites or manned space missions due to their high velocity. Thus, collisions are natural self-energizing generators for new debris. Models of future development have shown that atmospheric drag is insufficient to prevent a runaway process (known as 'Kessler Syndrome') in highly populated orbits.[5] Especially the orbits at a height of 800 km and 1500 km are affected, as these are some of the most densely populated areas. Protected zones have been defined in response to the increasing risk of collision. For satellites in these zones Fig. 1.2, certain guidelines have been established to suppress further exposure to objects. The guidelines include post-mission passivation operations and successful removal from protected regions within 25 years after end-of-life.[6][2, p. 21] For satellites in GEO raising the orbit into a graveyard orbit is the only feasible option. Satellites in LEO have the additional option of performing a de-orbiting maneuver to re-enter Earth's atmosphere.

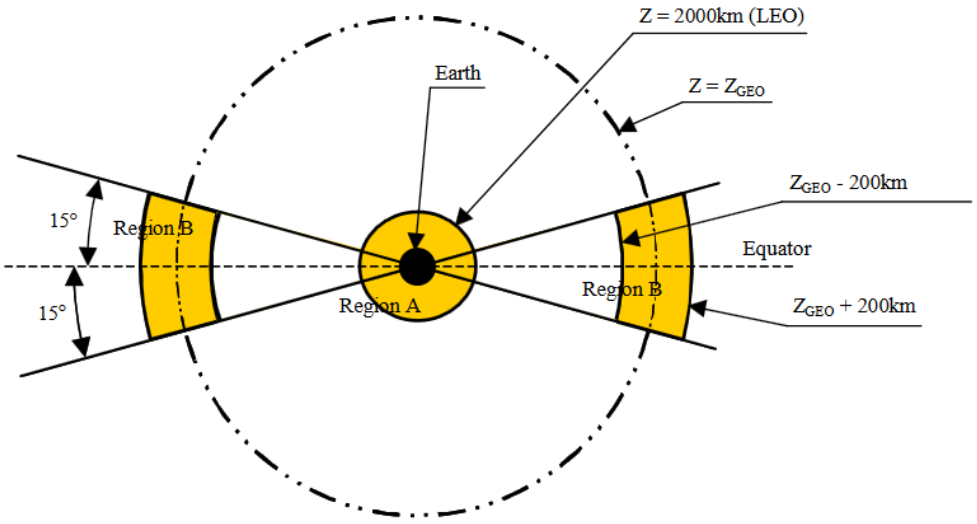

Figure 1.2.: Definition of the protected orbits. Region A is the LEO region and Region B is the geosynchronus region. [6]

Active debris removal (ADR) and on-orbit servicing for satellites are topics of current research.[7] ADR missions to de-orbit large pieces of debris, which pose the highest collision risks, are under consideration. Such missions would require precise information about the target, such as orbit properties, rotation frequency, rotation axes and used materials.[8]
The US Surveillance Network created and maintains a catalog of orbital objects in Two Line Element (TLE) format by using radar measurements.[2, p. 47 ff.] Each object in space has its own TLE entry in the catalog. As the TLE of an orbital object consists of several parameters that describe the object's trajectory, its position can be predicted for any given time based on the associated TLE. The TLE catalog is frequently updated and can be downloaded from the internet.[9]

For more detailed information about orbital objects, optical methods are used. Based on the position of the observer and the TLE data of the desired object, its trajectory in the reference frame of the observer can be predicted for an upcoming pass. This is then observed and tracked with a telescope. Active optical tracking is done by satellite laser ranging (SLR) stations which determine the distance between satellite and observer station by performing lidar measurements.[10] Recording telescope images of the object without an artificial source of light is considered passive optical tracking.
This thesis deals with the construction of a mobile system for passive optical observation. In the following it is referred to as Mobile Satellite and Debris Observation System (MS-DOS). Compared to an satellite laser ranging (SLR) station, the used equipment is less complex, less expensive and small-sized. Subject of investigation is the suitability of such an observation system for tracking orbital objects. In the case of successful tracking, the recorded data should be evaluated.
The time-changing brightness of an object can be extracted from the series of images recorded during passive optical tracking. In the context of astronomy and space debris observation, this dataset is known as light curve. Features and signal variations in a light curve have been used to deduce particular properties of observed objects.[11]
Calibrating the measured signal to magnitudes, the observed signal amplitudes become system-independent. This way, stereoscopic measurements with multiple observers would be comparable and might yield further target specific properties. The development of a suitable calibration process for the MS-DOS system is included in this thesis.
MS-DOS makes use of a color camera for tracking. Measurement of multiple wavelengths might yield information about the reflecting surface. Satellite construction relies on certain materials that are qualified for use in outer space. Similar to the concept of star color indexes and due to the given possibility of multispectral measurements, the ratio of the different color channels of the camera should be compared.[12]

2. Experimental setup

2.1. Hardware components

Figure 2.1.: The complete MS-DOS at observation site close to Stuttgart, Germany. The hardware components are introduced in the next picture.

As shown in Fig. 2.1, the entire measuring system is built on a cart which is stabilized by aluminum rails. A raised platform is in the middle on which the mount is installed. (Fig. 2.2 provides a better view and shows the construction inside the cart.) Attached to the cart are stilts to completely relieve the wheels and to further stabilize the system when performing measurements.

Fig. 2.2 shows the technical components of the tracking unit with labels for the individual components. The mount is a German Equatorial Mount from Astrosysteme Austria (ASA) called DDM60 Pro. It has a load capacity of 28 kg and uses differential encoders. Together with the mobile usage of the system, the differential encoders make it necessary to calibrate the telescope position before each series of measurements. For more information, see Sections 3.2 and 3.3. The equipment of the mount also includes a USB-stick with GPS capability for determination of time and location as well as the

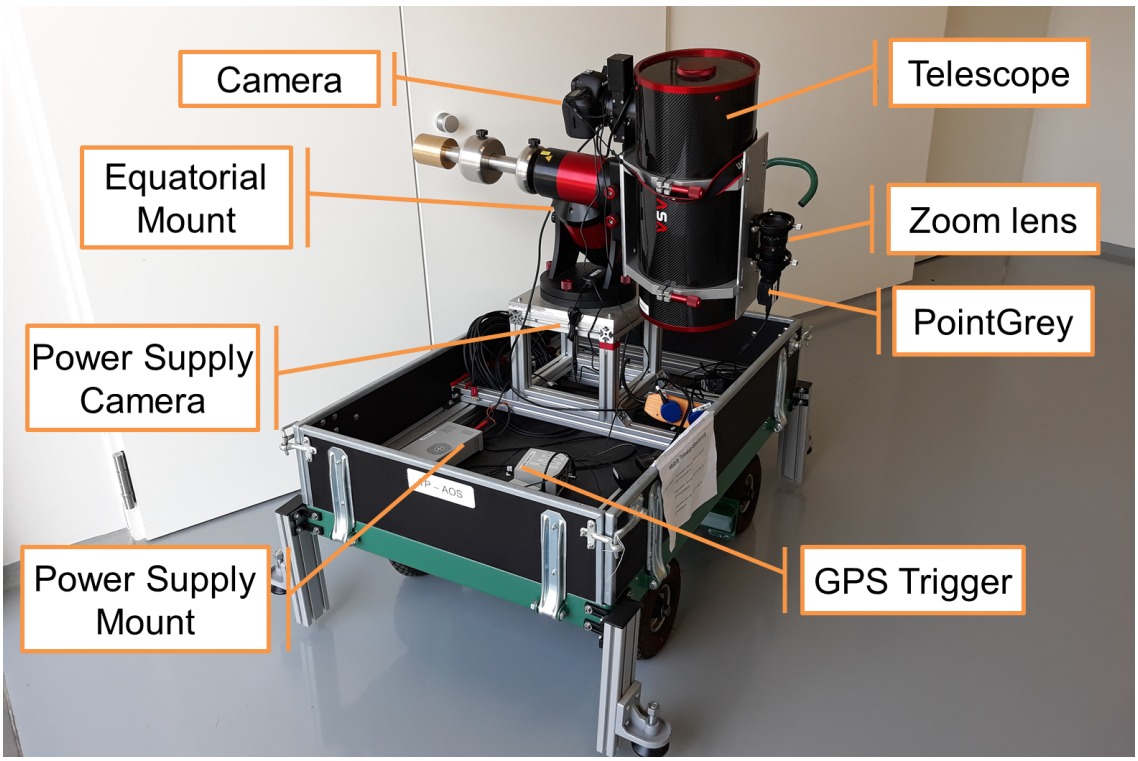

Figure 2.2.: Close up of MS-DOS with labeled components.

software package Autoslew for controlling the mount (see Section 3.2.1).
The mount is operated in conjunction with the ASA H200 Astrograph 8″ f2.8, which is a Newton telescope with hyperbolic mirror and a computer-operated focuser. As the name implies, the telescope has an aperture of 200 mm and a focal length of 560 mm.

A Canon EOS 5D Mark IV is used to capture the images. It is an off-the-shelf digital single-lens reflex camera (DSLR) released in September 2016. Compared to most cameras that for astronomical purposes, this camera is cheaper and has a three-color Bayer CMOS sensor (see Fig. 2.3). The sensor has 30 MP and a size of 36 mm × 24 mm, which corresponds to an average pixel size of 5.4 µm. The camera has an ISO standard range of 100 - 32,000 and an adjustable exposure time between 125 µs - 30 s.
The camera's hot shoe is connected to a trigger-box, which triggers when a recording is started. The trigger-box consists of a GPS receiver and an Arduino that returns the time-stamp of the current GPS time when triggered. Thus, for each image the exact time of the start of the recording is known, which is of importance for stereoscopic observations.
In the current configuration, the camera would bump against the mount in case of negative declinations. To prevent this, all telescope positions with negative declination are excluded in the software (see Section 3.2.2).
Another optical system is attached to the plate on the back of the telescope. This system consists of a PointGrey camera (GS3-U3-28S5M-C) and a zoom lens and is intended to assist as finderscope for the main system. The camera has a 2/3" sensor

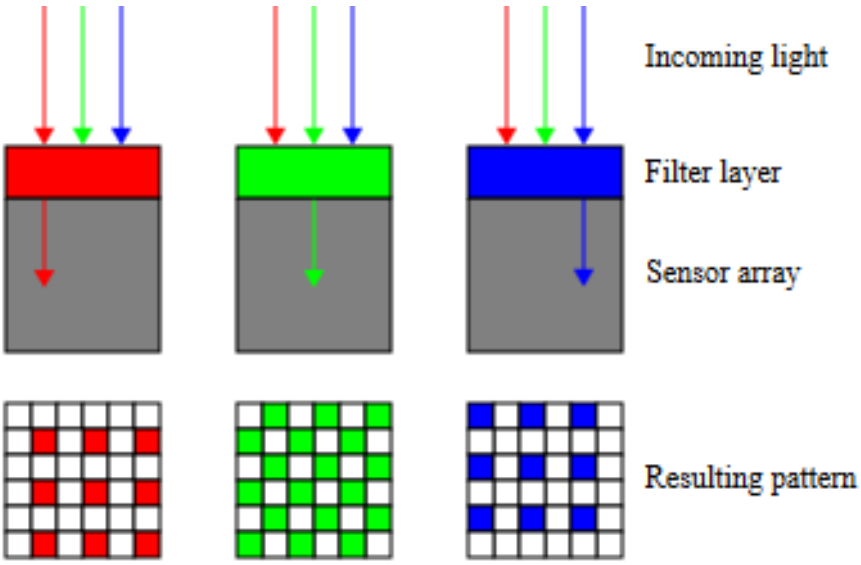

Figure 2.3.: Principle of Bayer sensor: The photosensitive cells on the semiconductor of a camera sensor can only detect brightness values. To obtain color information, a tiny color filter in one of the three primary colors red, green or blue is applied in front of each individual cell. In order to obtain the complete color image, the missing brightness values of the pixels are determined by digital image processing (different sorts of interpolation possible).[13][14]

(8.8 mm × 6.6 mm) and the focal length of the zoom lens is in the range of 12.5 mm - 75 mm, which are further specified in Section 4.2. The resulting values for the field of view (FOV) and the resolution of the images are discussed in Section 4.1.1.

2.2. Measurement site

The Institute of Technical Physics is located in Building H at the German Aerospace Center (DLR) site close to Stuttgart. Fig. 2.1 shows MS-DOS on the roof-deck of this building, where all the measurements were taken. Thus, the observer position lies at 48°44′55″ N, 9°6′9″ E at an altitude of 511 m above the WGS84 reference ellipsoid.
The institute is roughly 6.5 kilometers outside the city center of Stuttgart (see Fig. 2.4). Located even closer to Stuttgart is Uhlandshöhe Forschungsobservatorium (UFO), which is a SLR station that is also operated by the Institute of Technical Physics.[15]
Fig. 2.5 shows the surroundings of the measurement site. In the north of the roof, parts of the building greatly restrict the observable area of the night sky. The other structure in the south, on the other hand, is a smaller restriction on the available field of view, since the mount should not approach any negative declinations as described in the previous Section 2.1. Due to the structures and the balustrade, observations below 8° elevation in the horizontal coordinate system are hardly possible.

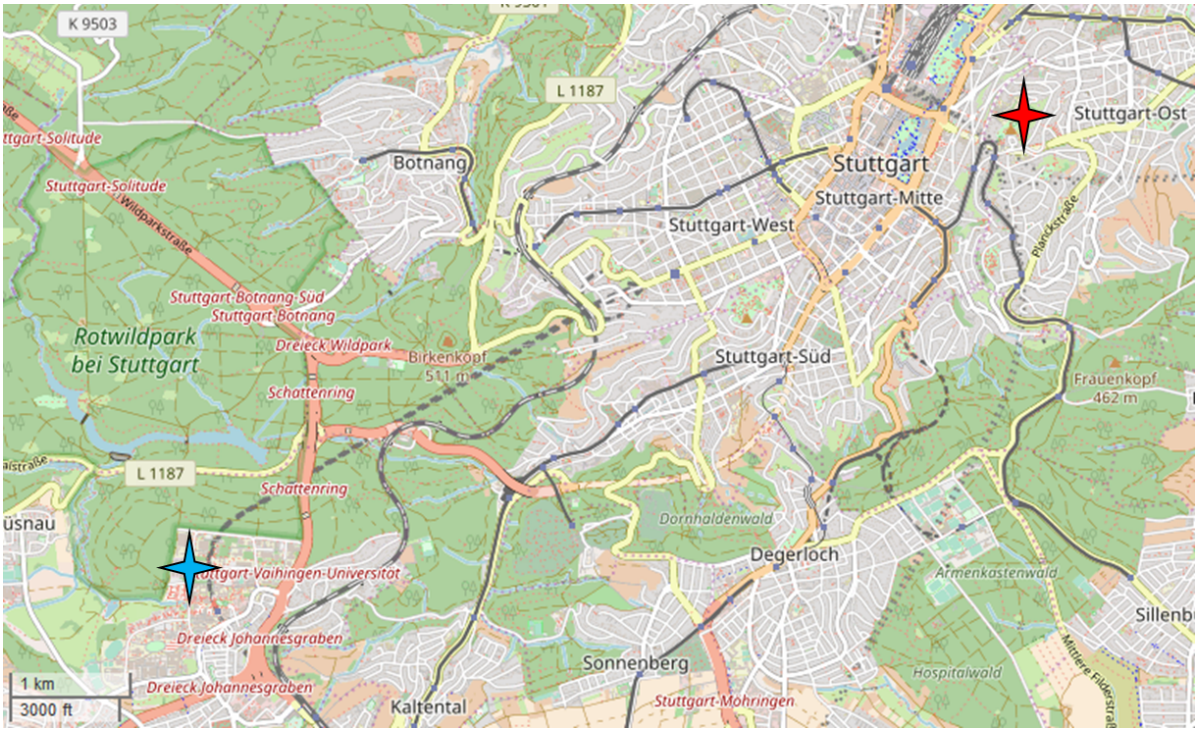

Figure 2.4.: Map of Stuttgart, Germany.[16] The position of the DLR Institute of Technical Physics is marked with a blue star. The red mark symbolizes a further observation site of the institute, Uhlandshöhe Forschungsobservatorium (UFO).

(a) View to the north.

(b) View to the south.

Figure 2.5.: Surroundings at the measurement site on the roof of the Institute of Technical Physics, German Aerospace Center (DLR) Stuttgart.

3. Software

3.1. OOOS

Managing the tracking and observation process of an orbital object is a complex task. In order to control a SLR station like UFO, the software tool Orbital Objects Observation Software (OOOS) was created by the Institute of Technical Physics at the DLR site in Stuttgart. It is a collection of Python scripts, designed to control a complete SLR station and capable of including new processes and hardware elements. Further improvements will be implemented with the goal of achieving autonomous operation.[17]
The current state of development allows full operation of UFO and over the past year new elements have been added that are crucial to the operation of MS-DOS. The elements described in Sections 3.2 to 3.4 are directly integrated into OOOS, while the LightCurveMaker2 (LCM2) module in Section 3.5 is a stand-alone program, which can be used to analyze the obtained image data.
As displayed in Fig. 3.1, the GUI of OOOS can be connected to various subprograms which are dedicated to control the needed hardware components for different tasks. A scheme of OOOS's information and data managment is given in Fig. 3.2.

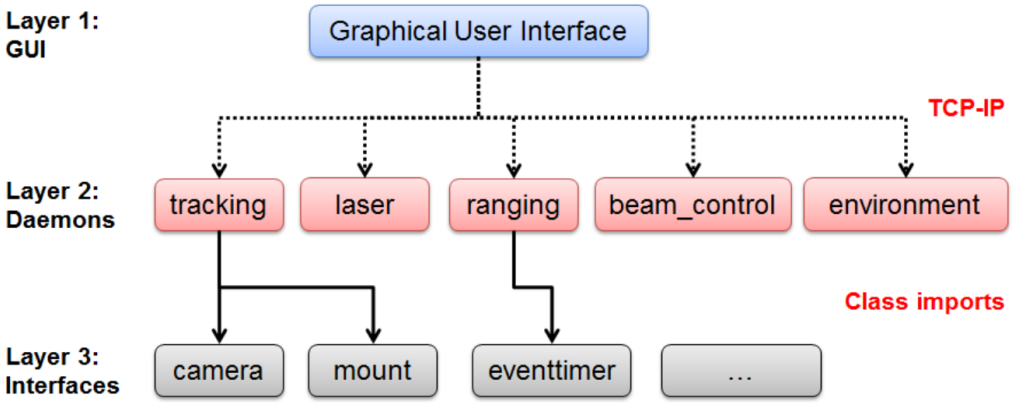

Figure 3.1.: Hierarchy of OOOS: control and interaction diagram. Depending on the measurement, the central GUI can be connected to its Daemons, which communicate with the hardware via interfaces. [17]

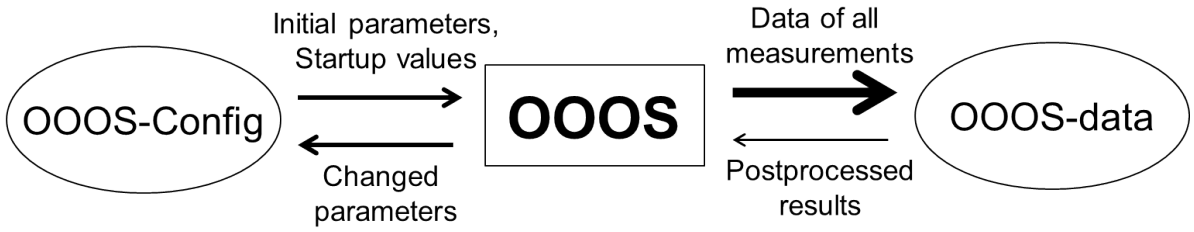

Figure 3.2.: Information exchange in OOOS environment. OOOS-Config stores parameters and settings, while in OOOS-data contains all the measurements from basic images to final analyses.

3.1.1. OOOS-Config and TLE

In OOOS-Config all the information is stored which is needed in OOOS. It is divided into measuring system settings ("system"), hardware ("hardware") and software parameters ("software"). The hardware parameters store important information such as the maximum velocity and acceleration of a mount (see Section 3.1.4).
As mentioned before, the latest TLE catalog is available on different websites in the internet. The user's login data for the website Space-Track.Org [9] are stored as software parameters in the local version of OOOS-Config. The TLE catalog should be updated at the beginning of each series of measurements. The further apart the TLE epoch and the requested point in time, the greater the uncertainty of the position that is calculated based on the TLE. After a few days, the actual position of the orbital object may already vary so much from the calculated position, that the target might no longer be in the FOV.[18]

3.1.2. OOOS-data

In OOOS-data the storage of recorded measurement data is organized. The data is sorted into folders where the first one is named after the date of measurement. The folder 2018-02-25 contains all measurements taken between 2018-02-25 08:00 UTC and 2018-02-26 08:00 UTC. The time interval is chosen this way to ensure that all measurements of one night are gathered in one folder.
The subfolders are the individual run folders and labeled as "runXXXX". Every time a new observation target is selected in OOOS, a new folder is created. Each run has a fixed substructure consisting of:

- **datalog**: Every log of the system is placed here. It contains, for example, the trajectory of the complete run, the log of the actual position in different coordinate systems, the offsets etc.

- **info**: The info folder contains information files for the target of the run, the pointing and for example the number of taken images. A whole copy of OOOS-config at the time of measurement is saved as well

- **results**: Output of offline analysis of the run is placed here
- **telescope-images**: All images taken with the tracking camera are saved here in FITS format (more on this in Section 3.4)
- **profiles, sequences, transmitter-images**: Folders that are not of interest for MS-DOS

3.1.3. Planning

Considering the eclipse and the objects height above the horizon, OOOS calculates the visibility of the possible targets, sorted according to their type (orbital objects, stars, planets etc.). The planning menu allows to queue multiple observation targets in one observation list. Assigned to the targets are time slots given as start and stop in UTC. When the complete automatization level is chosen, OOOS starts a new run when the observation start time is reached and tracks the current target until the observation time expires (see Section 3.1.4). This way, observations can be planned and scheduled for the whole night.

3.1.4. Tracking an object

Assuming a run on the star Vega is started in OOOS, the slew to Vega is calculated as trajectory. For this purpose the star's J2000 coordinates are converted into a current position (h, δ). As the current position of the telescope is taken at the same time, the start and end point of the trajectory are known. The aforementioned maximum velocity $v_{max}[^\circ/s]$ and maximum acceleration $a_{max}[^\circ/s^2]$ are obtained from OOOS-Config. Based on the start and end position as well as the boundary conditions in form of v_{max} and a_{max}, a trajectory is calculated. A trajectory consists of a series of points, where each point consists of a position and the timestamp when the mount should be at that position. Due to the boundary conditions, the approximate duration of the movement can be calculated, which in turn allows the proper movement of the target to be taken into account.
Assuming Vega is on the current pierside of the mount, a trajectory is then calculated which uses the shortest route to the destination. The telescope interface takes the trajectory points and calculates the angular velocity with which the axes of the mount must be moved.
Given the case that Vega is on the other side of the pier, a pier flip will be performed first. The mount is driven to a declination of 90°, then rotated around the HA axis till it matches h of the star, and from there to the desired declination δ. The individual axes are moved one after the other during the pier flip to prevent the hardware elements on the mount from crashing against the tripod.
The trajectory calculator is still active throughout the whole run and, due to the movement of the target, continuously calculates new adjusted trajectory points for the mount. As soon as the deviation between current target and telescope position falls below a limit,

the camera starts to take pictures (more on this in Section 3.4).
The procedure for tracking an object of a different type is quite similar to the example described above. For each target that is known in OOOS there is data regarding its position and proper motion. Despite the fact that the data is available in different forms, it can always be converted into a current position (h, δ) for the purpose of tracking. For example, stars are known through their entries in SKY2000 Star Catalog (Version 4), while satellites and space debris objects can be tracked with OOOS based on the TLE data provided by the United States surveillance network.[**SKY2000MasterCatalog**]
In the observer's horizontal coordinate system all of these targets might have different velocities, but the tracking approach is the same.

3.1.5. Closed-loop algorithm

An image analysis process is embedded in OOOS. The recorded images are scanned online for bright pixels which enables the measurement of an object's shift in the image position for a known movement of the mount. On supplying the current declination of an image, the transformation can be performed in both directions.
The Closed-loop algorithm (CL) is a PI controller. A set of parameters (minimum size, sigma above mean, maximum eccentricity) ensures that the user's desired object is recognized and selected as target (see Section 3.5). Corrections are applied to the mount axis based on the target's deviation from the center of the image, the observed declination and the specified control loop parameters. After slewing to the new position, the next image is evaluated with respect to the target's remaining deviation. CL is an iterative process which can drag an object from any point in the FOV into the center of the image (see Fig. 3.3).

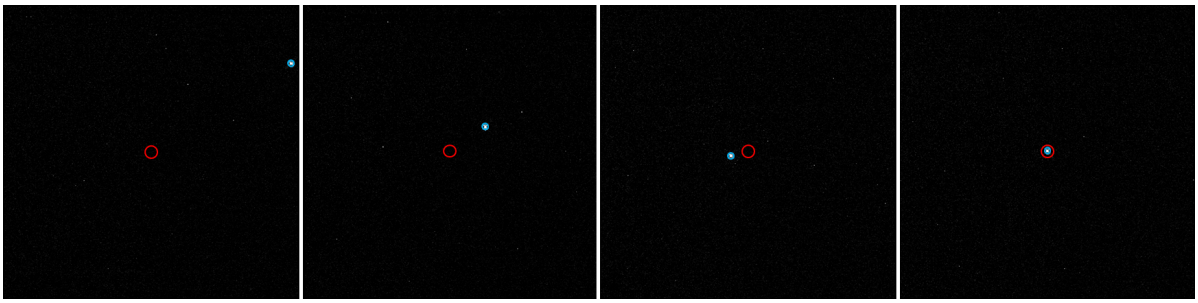

Figure 3.3.: Pulling Arcturus into the center of the field of view with the Closed-loop algorithm (2018-05-05, run0002, images 61, 63, 71 and 89). The red circle marks the image center, while the blue circle is drawn around the structure detected by the image analysis process. The blue circle was highlighted afterwards for better visibility.

3.2. Telescope-Interface

3.2.1. Autoslew and ASCOM

The ASA mount DDM 60 Pro comes with a control software called Autoslew. Autoslew is a handy tool for simple control of the mount (see Fig. 3.4). Functions such as checking the weight distribution when balancing the two axes are very practical to ensure a smooth observation routine. Furthermore, the ASA software ACC for adjusting the focuser is useful for setting up an optical observation system. However, since the mount is also supposed to be used for observing arbitrary orbital objects, an interface had to be created to control the mount via OOOS.

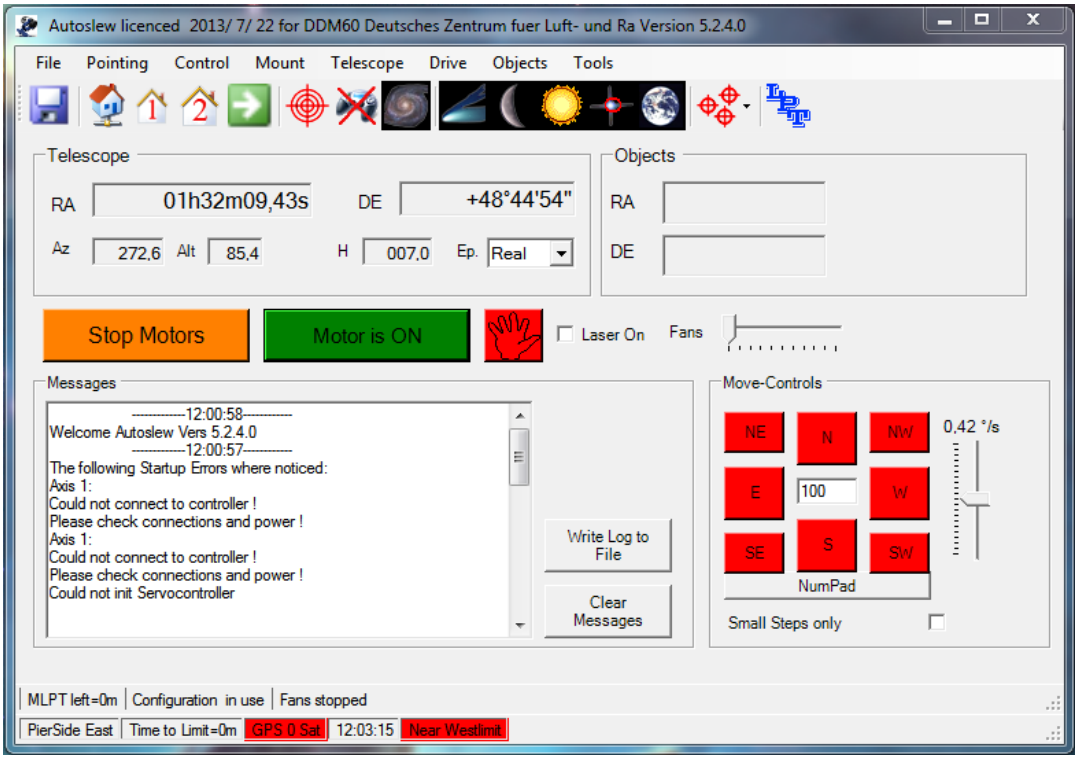

Figure 3.4.: Interface of ASA's software product "Autoslew" for controlling telescope mounts.

The ASA mount can be connected via ASCOM, where Autoslew serves as a COM object. ASCOM is language-independent interface for most astronomy devices that connect to Windows computers. The connection is then established by passing the program AstroOptikServer as a client to the Python module win32com. The mount can now be operated by using ASCOM commands.
At the beginning Autoslew needs information about its starting position and its axis speed. The ASA mount has direct motors, which is why the angular velocities of the

two axes are automatically measured at start-up as a function of the applied voltage. To determine the actual position, there is a reference mark on each axis which is registered very precisely when passing them. If the command HomeFind is given, the mount will try to find the reference marks by turning the axes a few degrees one after the other in both directions.
The reference marks are located near the parking position of the mount. In the parking position the telescope is located west of the mount and looks straight to the zenith (see Fig. 2.1).
Assigned to the reference position are celestial coordinates, which can be adjusted if necessary. Due to the differential encoders, the returned coordinates of the telescope position are determined by the offsets of the reference position.
In addition to the HomeFind command in the startup procedure, the telescope interface uses the Park command to automatically move the telescope to the parking position when disconnecting from OOOS. The most important commands for controlling the mount are the communication of the desired angular velocities on both axes and the request of the current coordinates and pierside. These commands are defined by ASCOM and they ensure that the alignment of the mount is known in OOOS at any time.
In addition to the normal tracking procedure described in Section 3.1.4, there is a PI controller that checks throughout the run whether the trajectory points were approached at the right time. The control loop adjusts the velocity which is calculated from the trajectory points.
These corrected angular velocities are then sent to the Autoslew program, which in turn ensures that the motors are supplied with the required voltage.

3.2.2. Exclusion regions

In the current configuration of MS-DOS with the Canon camera close to the mount, negative declinations cannot be observed. For this purpose, the system of specifying exclusion regions for individual mounts is added to OOOS. Trajectories which lead into a mount's excluded region are put on hold at the border of the defined region. This way, the mount can track an object as soon as it leaves the exclusion region without terminating the current run.

3.3. Pointing

3.3.1. Pointing model

During the construction and installation of a telescope, errors occur that cause the object you want to observe to not be in the center of the field of view of the telescope. Especially in the case of MS-DOS, which is moved between each observation night, the target might not be in the telescope's field of view and can only be found due to the finderscope. These pointing errors must be compensated by correcting the nominal

coordinates h and δ (see Eq. (3.1)). [19]

$$\begin{aligned} h' &= h + \Delta h(h, \delta) \\ \delta' &= \delta + \Delta\delta(h, \delta) \end{aligned} \tag{3.1}$$

with: h = true hour angle of object
δ = true declination of object

The pointing model ensures that the telescope is precisely aligned and that the object is as close as possible to the center of the field of view. Therefore, the pointing model's adjustment should be as consistent as possible with the necessary corrections of the celestial coordinates, Δh and $\Delta\delta$. When tracking orbital objects, the background seen in the images is constantly changing. Especially under these circumstances precise pointing makes it easier to identify faint objects.
In a classical pointing model there are six basic parameters. They are the static setup errors that can occur with an ideal telescope and are therefore referred to as geometric parameters. Both equatorial and azimuthal mounts have a set of six geometric parameters that are used to compensate the misalignment of the mount. Table 3.1 lists the geometric parameters of an equatorial mount.
If systematic deviations are still noticeable after applying this set of parameters, the

name	description	Δh term	$\Delta\delta$ term
IH	h index error	IH	
ID	δ index error		ID
CH	collimation error	$\mathrm{CH}\sec(\delta)$	
NP	h/δ non-perpendicularity	$\mathrm{NP}\tan(\delta)$	
MA	polar axis left-right misalignment	$-\mathrm{MA}\cos(h)\tan(\delta)$	$\mathrm{MA}\sin(h)$
ME	polar axis vertical misalignment	$\mathrm{ME}\sin(h)\tan(\delta)$	$\mathrm{ME}\cos(h)$

Table 3.1.: List of the geometric parameters for a classical equatorial pointing model.[20]

classic pointing model can be extended by additional parameters. A wide range of parameters with predefined correction terms can be found in literature. As each telescope has different site conditions and errors, it is also possible to define arbitrary parameters with new correction terms for special cases.[20]
In the case of the classic equatorial pointing model, the deviation in h depends on five unknown variables, whereas the deviation in δ has three variables (see Eq. (3.2)). To fully determine this system of equations, at least five stars have to be used to measure their deviations. The axis which has more dependencies dictates the minimum number of stars that have to be investigated. Respectively, the more complex the pointing model, the more stars are necessary to determine its parameters.

$$\begin{aligned} \Delta h &= \mathrm{IH} + \mathrm{CH}\sec(\delta) + \mathrm{NP}\tan(\delta) - \mathrm{MA}\cos(h)\tan(\delta) + \mathrm{ME}\sin(h)\tan(\delta) \\ \Delta\delta &= \mathrm{ID} + \mathrm{MA}\sin(h) + \mathrm{ME}\cos(h) \end{aligned} \tag{3.2}$$

3.3.2. Pointing model in OOOS

In order to apply pointing models in OOOS, a Python class called PointingModel was created. In this Python class any pointing model parameter (from literature and even custom definitions) can be used. As shown in Table 3.1, these parameters have a unique name, a description and correction terms for all axes to which they are applied.
A new pointing model is created by passing a file with measured values (h/δ), $(\Delta h/\Delta\delta)$ to the class and specifying which parameters should be used for the new pointing model. Assuming M parameters are used and the file originates from the measurement of N stars, then there are N observed deviations $(\Delta h/\Delta\delta)$ that are used to fit the pointing model. The M values of the pointing model parameters will be calculated using the least square method. The function f in Eq. (3.3) has to be minimized to obtain the best pointing.

$$f = \sum_{i}^{N} \sqrt{(\Delta h_{meas} - \Delta h)^2 + (\Delta \delta_{meas} - \Delta \delta)^2} \tag{3.3}$$

with: $\sum_i^N$ = sum over all N stars (for different (h/δ))
$\Delta h_{meas} = \Delta h_{meas}(h, \delta)$ = measured deviation, $\Delta\delta_{meas}$ analog
$\Delta h = \Delta h(h, \delta, p_j, ..., p_M)$ = fitted pointing model deviation, $\Delta\delta$ analog

Examples and plots of pointing models which were used are provided in Section 4.3.2.
Finally, the deviation Δh or $\Delta\delta$ for any position in the horizontal observer system can be obtained by just passing the according celestial coordinates (h/δ) to the pointing model class. The implemented pointing models are used to correct the positions in a given trajectory (see Section 3.1.4).

3.3.3. Telescope pointing interface

As described in Section 3.3.1, it is essential that a pointing model is created ahead of the actual observations to allow successful tracking of orbital objects with MS-DOS. The telescope pointing interface is an extension to the telescope control in OOOS in the form of a GUI. It is designed to automate the different steps in the process of creating a pointing model. Fig. 3.5 shows the layout of the telescope pointing interface.
On the interface, a desired number of stars can be set for a certain magnitude range. By executing the function "Select stars for calibration", all stars in the star catalog that are in the specified magnitude range and currently visible to the mount (10° over horizon, not in Exclusion Region), are listed. If less than the desired number of stars are visible, the magnitude range will gradually expand downwards until the specified number is reached. If too many stars are available, the stars with the shortest distance to their next two stars are removed one after another. At the end the predefined number of stars remains. The quality of the distribution in the night sky depends on the given set of parameters.
When activating the function "Make runs with", the selected stars are automatically approached and images are taken. Using the previously selected method, the deviations

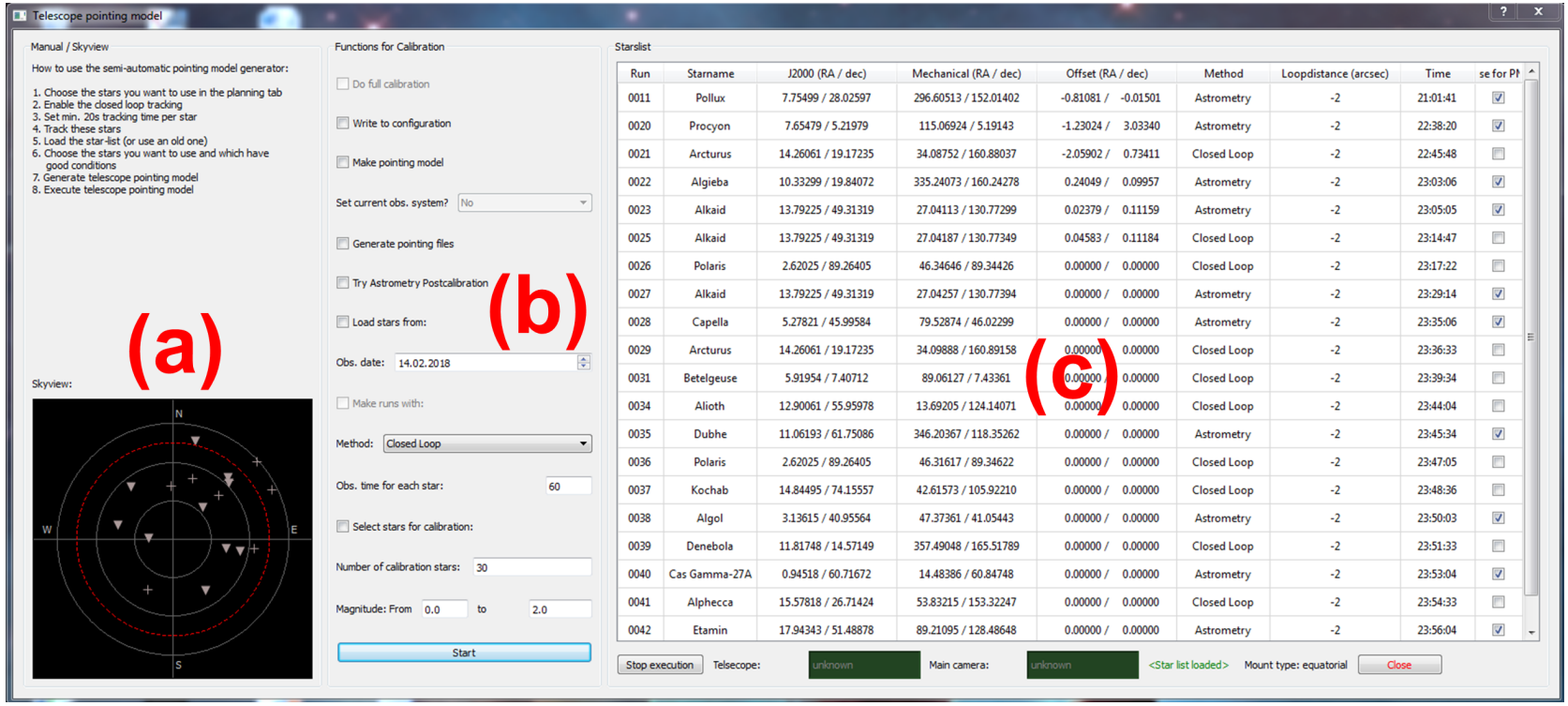

Figure 3.5.: The telescope-pointing interface as extension to the OOOS GUI. (a) is the Skyview plot of OOOS which represents the horizontal coordinate system of the observer. The functions and parameters that are used in the process of generating a new pointing model are in the same column as (b). In (c), all star runs of a selected night are listed with their relevant information. The position of each star at the time of measurement is displayed in (a). Runs where the option "Use for PM" is ticked, are marked with triangles in (a), while the others are marked with crosses.

Δh and $\Delta\delta$ of the star from the approached position can now be determined. The Closed-loop method (Section 3.1.5) is useful when the pointing is so precise that the stars are already in the field of view of the main telescope. If this is not the case, the method "Astrometry" should be selected. This method uses the taken images and the approximate orientation of the telescope to determine the celestial coordinates of the center of the images via PinPoint Astrometric Engine by DC-3 Dreams. It requests the resolution of the image in FOV_{pixel} (Section 4.1.1) and a search center in J2000 coordinates in addition to the image itself. The star constellations found in the image are compared to cataloged stars in a certain range around the search center. Therefore, the approximate orientation of the telescope needs to be known beforehand. When the stars in the image can be matched, the difference between the celestial coordinates of the image center and the star position is applied as an offset to the trajectory.
The duration of a run is fixed and can be set in the GUI. After the time has elapsed, the observed star is in the middle of the images and both sets $h', h, \Delta h$ and $\delta', \delta, \Delta\delta$ are saved.
In order to be able to flexibly access old as well as new measurements, there is the function "Load stars from". All runs on stars made during the selected night will be displayed with the additional option "Use for PM" on the far right of the list.
The method "Generate pointing files" generates a text file with the values (h/δ), $(\Delta h/\Delta\delta)$ of the runs that are marked as "Use for PM". The method "Make pointing model" makes use of the class PointingModel to calculate a pointing model based on the previously generated file. Used are the pointing model parameters which are currently applied to the connected mount and deposited in OOOS-Config. After performing the fit, there are new values for the pointing model parameters available.
The parameter values in the OOOS-Config section of the connected mount can then be updated to the new values via "Write to config". At the next restart of OOOS, these parameters are used for the pointing model that will be applied to the trajectories.

3.4. Camera-Interface

Many camera manufacturers provide a software development kit, abbreviated SDK, for the software-based control of their cameras. Typically an SDK includes one or more APIs, programming tools, and documentation. Every SDK has its own concept for controlling the hardware. Accordingly, an SDK may be suitable for different applications in different ways. In the case of Canon, there is an official SDK called EDSDK that can be used in combination with most of their products.
The Canon camera supports a variety of

format	image size in pixels
RAW / JPEG L	6720×4480
mRAW	5040×3360
sRAW	3360×2240
JPEG M1	4464×2976
JPEG S1	3360×2240
JPEG S2	1696×1280

Table 3.2.: Available outputs

output formats shown in Table 3.2. It can deliver images in both JPEG and canon raw image (CR2) format. Working with JPEG images is not an option in the case of MS-DOS. JPEG is a lossy compression of images which is applied to achieve a reduction of the acquired memory capacity when storing them. The compression results in a loss of information that interferes with the subsequent calibration to apparent magnitudes. This is why raw images are used here. The CMOS-sensor output is a 12 bit RGB signal. As mentioned in Section 2.1, the CMOS-detector has a size of 36×24 mm and a pixel size of 5.4 µm, thus having 6720×4480 pixels in its biggest format (RAW). In the end the sRAW format ("RAW with initial binning 2") was chosen because it occupies less space on the hard drive and the further processing steps are a lot faster than for a full sized RAW image.

3.4.1. Capturing images with EDSDK

In the following, the control of the camera using the EDSDK will be explained. First, the camera is found by its COM connection and then integrated into a computer-controlled session. Once the camera is integrated in a session via the created camera interface, it can be controlled directly by OOOS. This includes sending commands but also setting and querying camera parameters.
To capture an image, parameters like the shutter speed and ISO are set first and then the command to trigger is sent. At the same time, further image parameters such as the name of the camera from the camera interface or the current celestial coordinates from the telescope interface are buffered in OOOS. These parameters include all the information needed to evaluate the data, for example, the GPS time of the trigger module as described in Section 2.1.
There are two more parameters for the camera, the region of interest (ROI) and the binning factor b_n, that determine the desired region and resolution of the image. Only this specified region is later saved in the FITS images which are subsequently processed by OOOS while the rest is discarded. In the optimal case, these parameters can directly be passed on to the camera via SDK to obtain the desired array from the sensor. However, due to the concept of EDSDK an image must first be completely saved as a CR2 file before the data can be accessed. Even if only a small part of the image is needed, a lot of unused data has to be processed and the following steps take unnecessarily long.
Once the camera has finished exposing and reading the sensor, the image data is stored on the host computer via a file stream. For an image with one second exposure the download starts 1.6 s after the capture has been triggered, indicating that the processes subsequent to the end of exposure (e.g., reading the sensor) take roughly 600 ms. Due to the USB 3 connection, the download of a typical sRAW image with about 10 Mbytes is performed within 0.4 s.
Once the image is stored to the hard drive, the camera is able to start the exposure of the next image and another thread is responsible for processing the latest raw image. This process saves the data array of each image in FITS format and subsequently adds the previously chached parameters as header information.

To obtain data arrays from the stored sRAW images, the module rawpy is used. This is a Python module that can read CR2 formats and returns a 3D array after applying a post-processing function to the raw data. The parameters for the post-processing are chosen in such a way that the conversion of the sRAW image is linear and the 12 bit camera pixel values are adjusted to 16 bit color information on each channel. Additionally, the conversion makes use of the adaptive homogeneity-directed demosaicing algorithm to calculate the missing pixel values due to the Bayer pattern.[21] To avoid misunderstanding, from now on the output of a pixel is described as Analog Digital Unit (ADU). This results in an output array with $3660 \times 2240 \times 3$ entries and ADUs in the range of 0 to 65535. Opening a sRAW image with 10 Mbytes takes around 600 to 800 milliseconds, strongly depending on the size of the array inside the CR2 image. Unlike the CR2 format, FITS images are easier and faster to open.

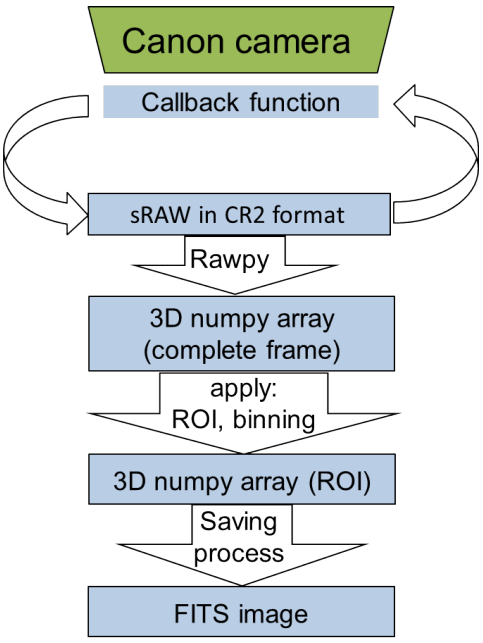

Figure 3.6.: Process of saving captured images.

The aforementioned region of interest and binning are applied in the next step. This means the unneeded part of the image can be discarded in case of the Canon camera. The ROI (e.g., 1000×1000) defines the number of the innermost pixels taken from the middle of the image array. After that, the binning factor b_n is applied to the region of interest, reducing the noise level and the size of the final FITS image by taking the average over $b_n \times b_n$ pixels. For more information regarding the field of view, see Section 4.1.1.

The image information is now available with all additionally stored parameters as a FITS image and can be used for later analysis. These images are stored in the data folder of OOOS.

3.5. LightCurveMaker2

The GUI LightCurveMaker2 (LCM2) is intended to evaluate images taken with OOOS. If a run folder is selected in LCM2, all FITS images that are in that folder will be rendered in a list. On selecting an image in the list, it will be displayed in the view-box on the left and analyzed. LCM2 works with a modified version of the image-analysis-process, which is already used in OOOS (see Section 3.1.5).

The first step in image analysis is to read in the data array as well as the header of the image. The next step is to determine the background. For this purpose, the median is determined from the ADU distribution of the entire image area. A histogram is created,

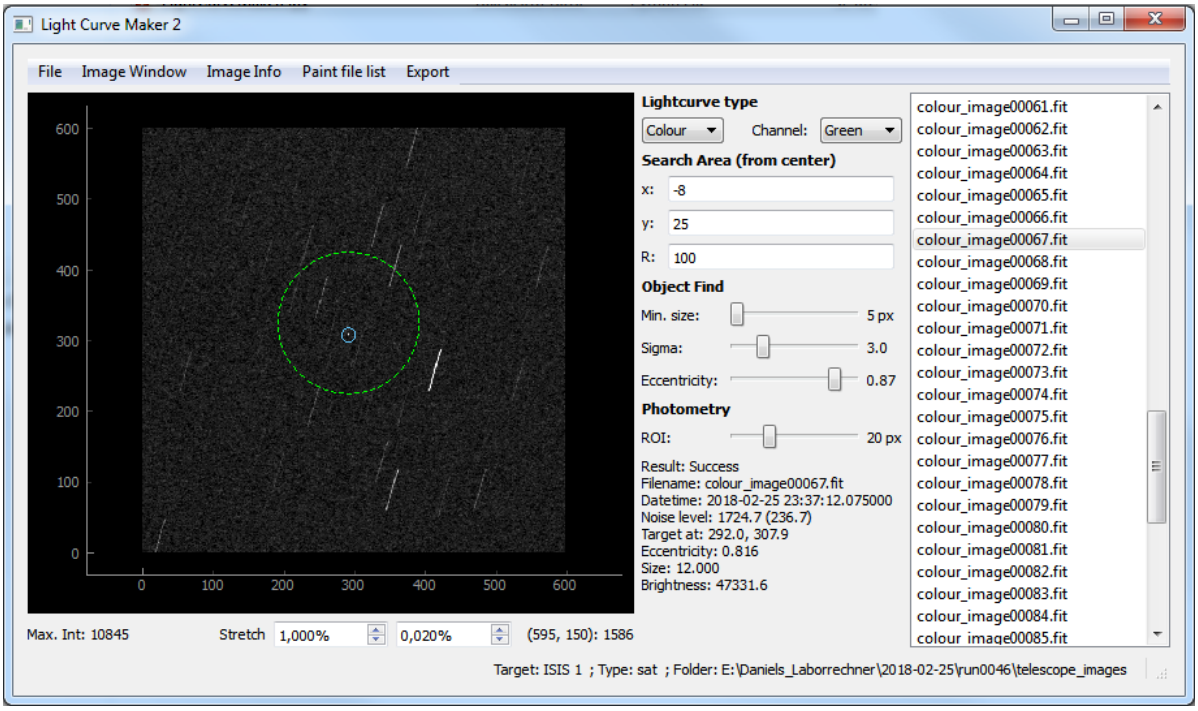

Figure 3.7.: Shown is the GUI of LightCurveMaker2. The selected example is the green color channel of the 67th image taken at this specific run. All following figures in this Section are concerning this image.

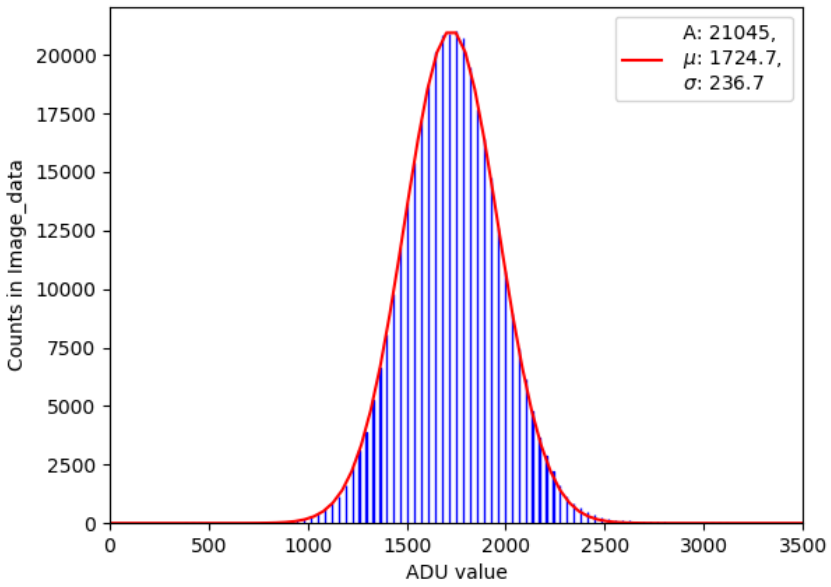

Figure 3.8.: Histogram of the green color channel of an image. Integrated in the plot is the fitted Gaussian curve with the amplitude A, the mean value μ and the standard deviation σ. Output of LCM2 →Image Info →Hist/Noise.

which contains all ADU values between 0 and roughly twice the median. For a typical picture of MS-DOS in the resolution 600 × 600 pixels, more than 99.5 percent of the ADUs are recorded in the histogram. A Gaussian curve is fitted to the histogram, which yields the mean μ and the standard deviation σ of the image background.
The main purpose of LCM2 is to detect the target in an image. In order to be able to restrict and influence the search for the target, the following parameters are used:

- **x**: center coordinate of search area (shifted from the image center)
- **y**: center coordinate of search area (shifted from the image center)
- **R**: radius of search area
- **Min. size**: number of contiguous pixels, current value referred to as N_{min}
- **Sigma**: specifies sigma above mean, current value referred to as sig
- **Eccentricity**: maximum eccentricity, current value referred to as E_{max}

x, **y** and **R** determine the search area, which is illustrated by the green dashed circle in Fig. 3.7. First, sig is used to determine the threshold $ADU_{min} = \mu + sig \cdot \sigma$. The

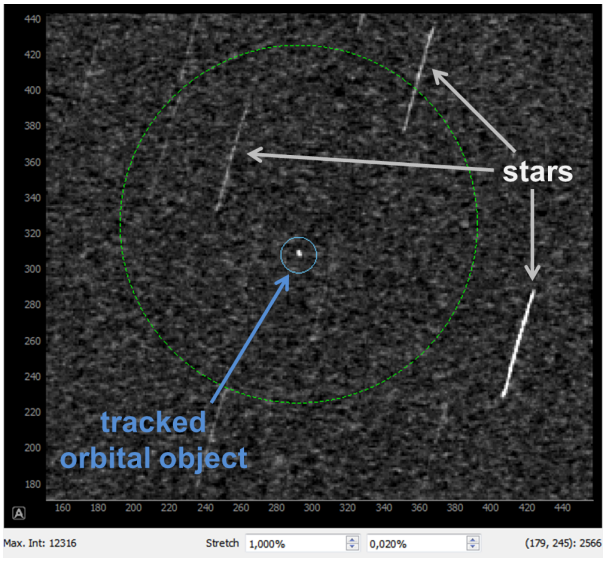

(a) Magnified view of the image presented in the LCM2 GUI in Fig. 3.7.

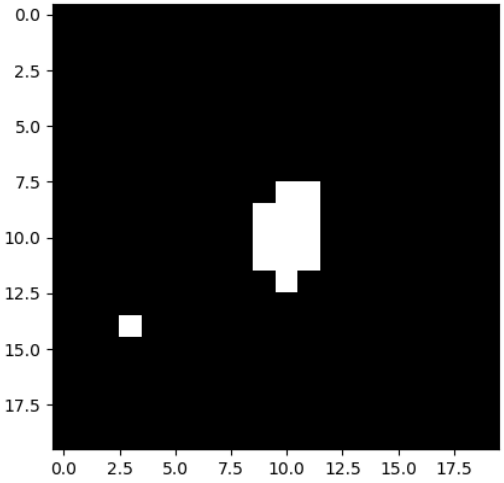

(b) Bool image of the target (number of pixels on both axes) is created by applying the threshold $ADU_{min} = \mu + 3.0 \cdot \sigma = 2434.8$ to the original image.

Figure 3.9.: Detection of structures with LCM2. Especially the determination of the target structure is complicated with MS-DOS images as the target consists only of a few pixels due to the focal length of 560 mm.

image is then scanned for locations where several contiguous pixels are brighter than this threshold ADU_{min}. The detection algorithm works similar to Fig. 3.9b. These groups

of contiguous pixels are referred to as structures, which have certain parameters such as center of gravity, maximum pixel brightness, size, etc.. Of the structures found, only those are saved which fulfill the following conditions: they must consist of more pixels than the minimum size N_{min}, they must lie within the defined search area and must not exceed the maximum eccentricity E_{max}. From the set of structures that meet the requirements, the one containing the largest maximum ADU is selected and declared as the target structure. In most cases, the tracked object can be found in this way, as other light sources, such as stars, degenerate into streaks due to the tracking movement during the exposure time. If the correct target is still not found, the user can manually select any location in the image and set it as the target structure. The blue circle in Fig. 3.9a indicates that a target structure is found.
Another parameter can be set in LCM2 for the process of determining the brightness of the target structure:

- **ROI**: edge length of ROI in pixels, current value referred to as l_{ROI}

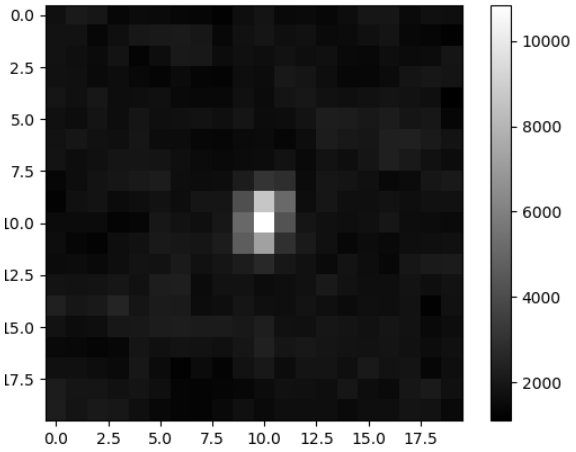

Figure 3.10.: ROI around target structure.

Note, that this parameter is defined the same way as the ROI in Section 3.4, but has nothing to do with the process of capturing images. A square with the edge length l_{ROI} and the center point in the target structure's center of gravity is now defined as ROI. In Fig. 3.10 this ROI is shown as an example. Showing the ROI is an implemented function in the GUI to check the output. The signal of the target corresponds to the ROI without background and can be calculated with Eq. (3.4). Since the background was determined using the entire image, this method cannot be applied if the background of the image has gradients.
In the case of multispectral observations, the 2D array of the green color channel is scanned and the position of the obtained target structure is used to define the ROI for all color channels. The resulting signals are calculated with the individual mean value of the color channel's background. LCM2 stores the header information and the results of the analysis for each image.

$$I = \sum_{ROI} ADU - \quad l_{ROI}^2 * \mu \tag{3.4}$$

with: I = brightness of the target
$\sum_{ROI} ADU$ = cummulated ADU in the defined region of interest
l_{ROI} = current edge length of ROI in pixels
μ = mean background of image

A light curve maps the temporal brightness fluctuation of an orbital object.[ref to a source] Thus, a light curve can be created with the LCM2 by combining the image's UTC timestamp and the observed signal.
The signal of the green color channel can be converted to apparent magnitudes $magn_V$. The process is defined in Section 4.1.7. In the case of color images, the color channels relative to one another can be evaluated as described in Section 4.1.6.

4. System characterization

4.1. Main optical system

To obtain reliable information about the observed orbital objects, there are various things that need to be considered. This section is dedicated to the discussion of the optical properties of MS-DOS and to characterize the recorded images of orbital objects.

4.1.1. Field of view

The size of the field of view (FOV) of a given optical system can be calculated using Eq. (4.1).[22] Thus, the average FOV of each pixel (FOV_{pixel}) corresponds to Eq. (4.2).

$$FOV[^\circ] = 2 * arctan\left(\frac{p * I}{2 * F}\right) * \frac{180}{\pi} = 2 * arctan\left(\frac{S}{2 * F}\right) * \frac{180}{\pi} \tag{4.1}$$

$$FOV_{pixel}[''] = 2 * arctan\left(\frac{p * I}{2 * F}\right) * \frac{180}{\pi} * \frac{3600}{I} \approx \frac{p}{F} * \frac{180}{\pi} * 3600 \tag{4.2}$$

with: FOV_{pixel} = FOV of each pixel, given in arc-seconds
FOV = field of view in degree
p = pixel size, mm per pixel
I = image size in pixels
F = focal length in mm
S = used sensor length in mm

The ROI and the binning factor b_n mentioned in Section 3.4 have a huge impact on FOV and FOV_{pixel} of the final FITS images.
Generally spoken, discarding pixels in the exterior of the camera sensor narrows the FOV of the optical system while FOV_{pixel} stays the same. In the case of the Canon camera, every given ROI smaller than 3360×2240 pixels reduces the effective field of view. Binning on the other hand only increase FOV_{pixel} by averaging over $b_n \times b_n$ pixels while the value FOV is constant.
This is why using the sRAW format has the same effect as applying a binning of 2 to the RAW format and taking this as image source (see discussion about RAW formats in Section 3.4). Working with sRAW reduces the effective number of pixels to 3360×2240 while the overall FOV stays the same. In order to optimize the saving process, it makes sense to use the sRAW format.
In OOOS, different combinations of ROI and b_n can be saved as presets in the camera

control terminal. Section 4.1.1 presents the properties for frequently used camera presets. Of course any other set of parameters can be used, but the presented sets are well suited for most cases.

When calibrating the telescope's celestial coordinates, a ROI of 2000 × 2000 pixels is used to have a relative great FOV. Aside from this, the observation of orbital objects is often done with a ROI of 600× 600 pixels and without averaging ($b_n = 1$). The small FOV is chosen because the observed object is already close to the center of the image. A greater field of view would only lead to saving additional star stripes in the exterior region of the recorded images while observing satellites or space debris.

Camera presets		Image properties	
ROI	b_n	$FOV[^\circ]$	$FOV_{pixel}["]$
3360 / 2240	2	3.711/ 2.475	3.98
3000 / 2100	3	3.314/ 2.320	5.97
2000 / 2000	2	2.097/ 2.097	3.98
1000 / 1000	2	1.105/ 1.105	3.98
600 / 600	1	0.663/ 0.663	1.99

Table 4.1.: Available camera preset parameters and their resulting FOV as well as FOV_{pixel}.

4.1.2. Post-processing

For digital images there are a number of different sources of noise. Considering the most prominent sources, each digital image supplied by a camera sensor is a combination of bias, dark current and the desired signal. The issue is well known among astrophotographers and handled by image post-processing, which usually consists of dark and flat correction.
The bias is system-dependent but neither temperature nor time dependent. The dark current on the other hand is both temperature and time dependent. The dark frame (an image where the camera is completely protected from any light) is solely a sum of bias and dark current. The raw image data is then subtracted by the dark (process is called image dark).
Theoretically, only the pure signal should be left, but there is another source of errors: heterogeneity of the pixels (pixel noise) and dirt on the optics. This effect is determined by taking a flat (an image of a uniform illuminated field). Then the image dark is divided by the flatdark, which is the flat subtracted by the dark. The result is the corrected raw image, which can then be further processed.
The whole process of dark and flat correction is expressed mathematically in Eq. (4.3).[23] In order to check the impact of image post-processing on the magnitude calibration, flat and darks were recorded with MS-DOS.

$$S(x,y) = \frac{R(x,y) - D(x,y)}{F(x,y) - D(x,y)} \tag{4.3}$$

with: S = post-processed image
R = raw image
D = dark
F = flat

The darks are recorded in the night with the end cap placed on the telescope to prevent any light from illuminating the sensor. The dark current is negligible small for all observed parameter combinations ISO and exposure time ($ADU_{avg} \ll 100$). This simplifies Eq. (4.3) to $S(x, y) = R(x, y)/F(x, y)$.
The flat is captured by recording the clear sky shortly after dawn (see Fig. 4.1). Due to the pointing model and the Closed Loop-algorithm (both in Chapter 3), celestial and orbital objects are always at a central position of the taken images. Thus, in the case of the magnitude calibration, only the pixels at the center of the sensor are illuminated by the light of the observed target(s). Taking the typical ROI of 600×600 pixels and normalizing the flat to the maximum ADU in the ROI, yields Fig. 4.2 which proves, that the used region at the center of the camera sensor is mostly uniform. A flat correction is therefore not necessary.
Respectively, there is no need for post processing and correcting the raw images when the magnitude calibration and the subsequent observations are restricted to the smallest predefined ROI of 600×600 pixels.

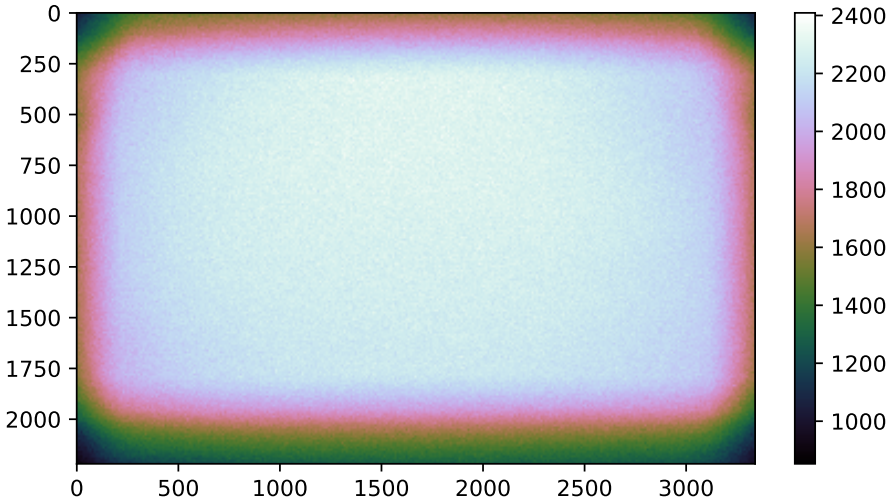

Figure 4.1.: Calibration factor indicated by its pixel position on the full frame.

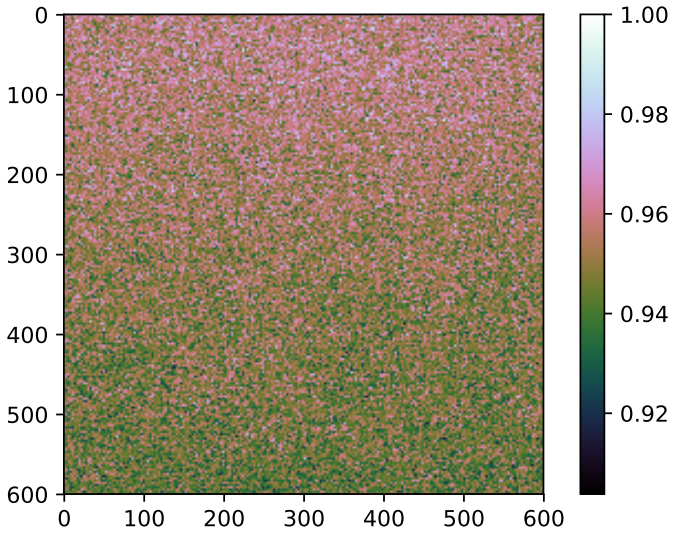

Figure 4.2.: Calibration factor for the typical ROI of the innermost 600 pixels.

4.1.3. Inherent uncertainty of measured signals

Various statistical error sources for the measured brightness signal of MS-DOS are possible, such as an inaccurate shutter time of the sensor hood or a varying determination of the image background. To check the reliability of the output of camera and LightCurveMaker2, a constant light source is first observed for a longer period of time. In this particular case, it was a screen that was black except for a white dot in the middle. The system was located in a completely darkened room for the measurement.
In Fig. 4.3 the evaluated distribution of the measured values for the green color chan-

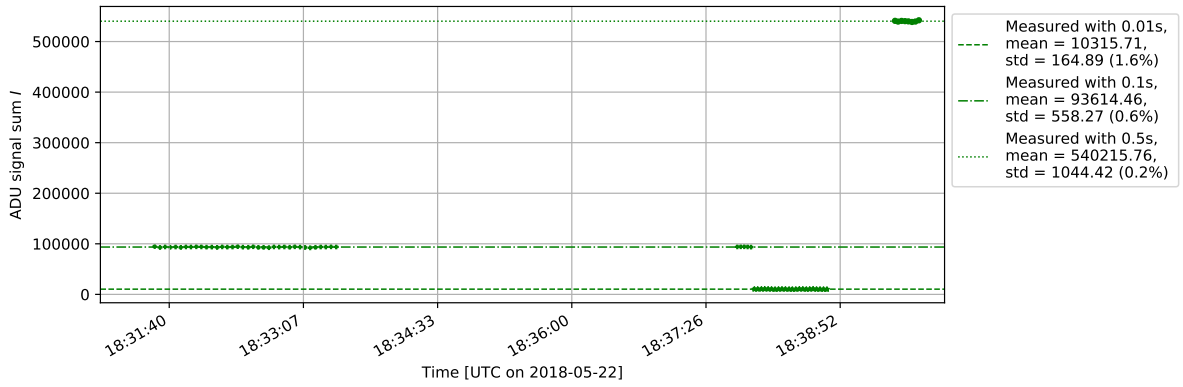

Figure 4.3.: Measured signal I of the artificial light source with ISO 800 for the green channel and different exposure times.

nel is shown. The results of all color channels are given in Table 4.2. The maximum fluctuation of 1.6 percent occurs for the measurement with the shortest exposure time. Accordingly, the hardware's accuracy is sufficient for tracking orbital objects.
Next, the system is tested under real conditions by observing a star for ten minutes. Except for the tracking of the star, the telescope does not move to allow an undisturbed measurement. Fig. 4.4 shows the long-term measurement, which was only influenced by a doubling of the exposure time in the middle of the observation. HD 159542 and the exposure times were chosen this way as the conditions for tracking satellites are similar.

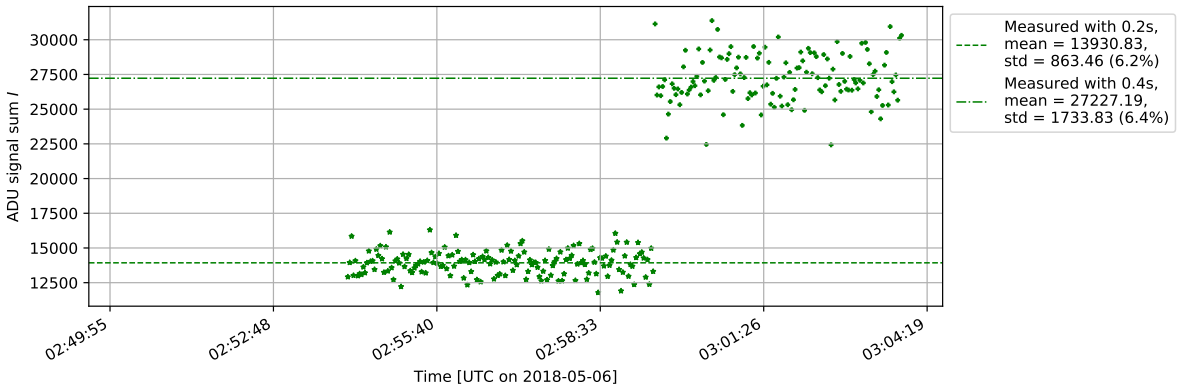

Figure 4.4.: Measured signal I of HD 159542 with ISO 800 for the green channel. Exposure time changes from 0.2 s to 0.4 s at 02:59:30 UTC.

Although the star radiates with constant intensity, the output signal of the system is noisy. The typical observed standard deviation is more than six percent of the mean value. The only difference to the previous measurement in the darkened room is that here the atmosphere has a decisive influence. For all measured brightness values of celestial and orbital targets, a fluctuation of roughly five to ten percent has to be expected (see Table 4.2).

	standard deviation for	
color channel	artificial (light source)	star (through atmosphere)
red	$375 \equiv 3.7\%$	$3474 \equiv 10.0\%$
green	$165 \equiv 1.6\%$	$1734 \equiv 6.4\%$
blue	$272 \equiv 2.9\%$	$2039 \equiv 10.5\%$

Table 4.2.: Maximum observed values for the ADU standard deviation at different exposure times. All measurements are performed with ISO 800.

4.1.4. Linearity in exposure time and gain

For the magnitude measurement it is essential to avoid overexposure of the detector pixels. To be more specific the camera needs to be operated in a region where incoming signal and ADU output are related linear. An ideal camera is linear in the complete ADU range. In the case of the 16 bit FITS images, this would correspond to linearity up to $ADU_{threshold} = 65535$. The ISO corresponds to an internal sensor current multiplier of ISO/100. In the ideal case, doubling the exposure time or the ISO value would result in doubling each pixel's ADU as long as the resulting ADU does not exceed $ADU_{threshold}$. In the case of MS-DOS, the first step is to check for which combinations of ISO and exposure time the detector output is linear to the input. Any star can be used to investigate the linearity of the camera sensor as long as the star is located in the middle of the field of view during the measurement (see Section 4.1.2). The aim is to record the ADU of the brightest target pixel (in the following called ADU_{max}) for each parameter combination ISO and exposure time.
In the following example, star Tau Herculis with a magnitude of $magn_V = 3.9$ was chosen for the measurements. A small python script controls the measurement and changes the parameter combination every ten images.

- **ISO:** 200, 400, 800 and 1600
- **exposure time [s]:** 1, 0.5, 0.4, 0.3, 0.2, 0.1, 0.05, 0.025, 0.02, 0.01, 0.005, 0.0025, 0.002, 0.001, 0.0005, 0.0002

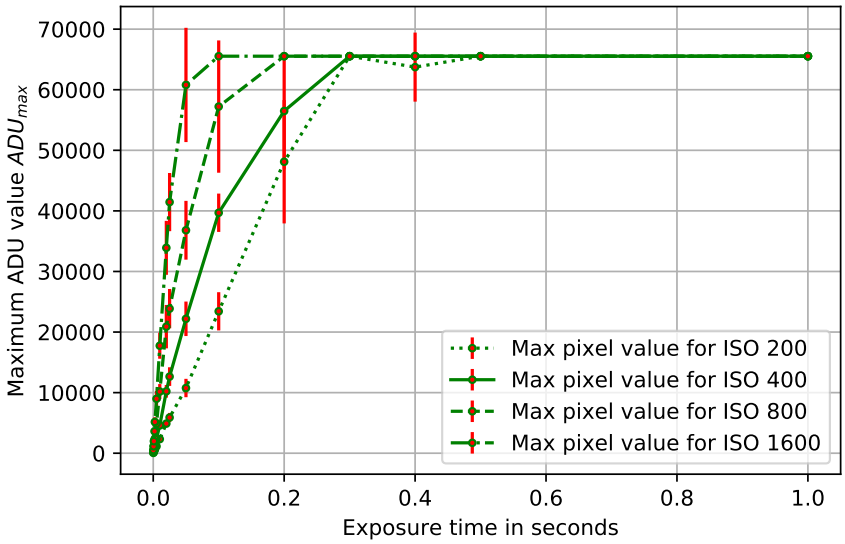

Figure 4.5.: ADU_{max} plotted against exposure time for Tau Herculis. As expected, the measurements converge to 65,535 for long exposure times.

This way, for each given ISO and exposure time the same number of images is analyzed. Additionally, each color channel of the camera is investigated separately. Thus, for each

parameter combination and color channel, there is a mean value and its standard deviation (see Eq. (4.4)).

$$\bar{x} = \sum_{i=1}^{N} x_i, \qquad \sigma_x = \sqrt{\frac{\sum_{i=1}^{N}(x_i - \bar{x})^2}{N-1}} \tag{4.4}$$

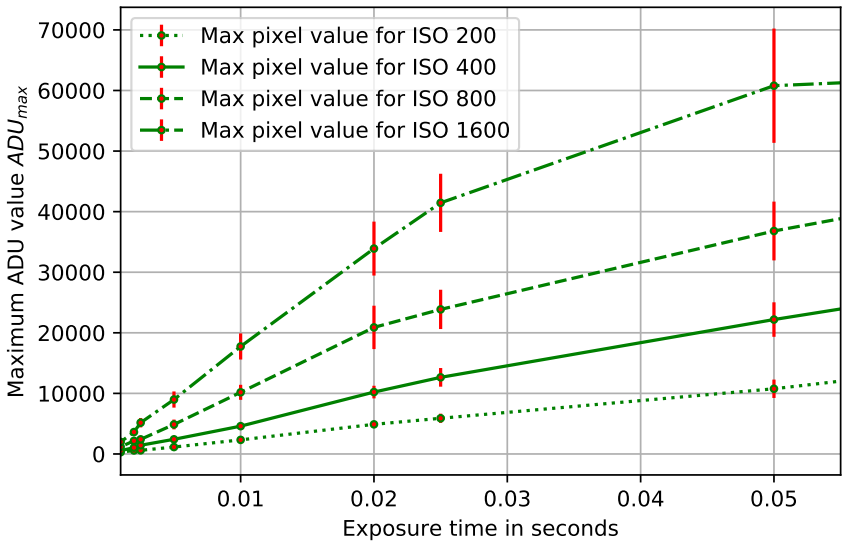

Figure 4.6.: ADU_{max} plotted against exposure time for Tau Herculis. Only the desired range of exposure times is shown.

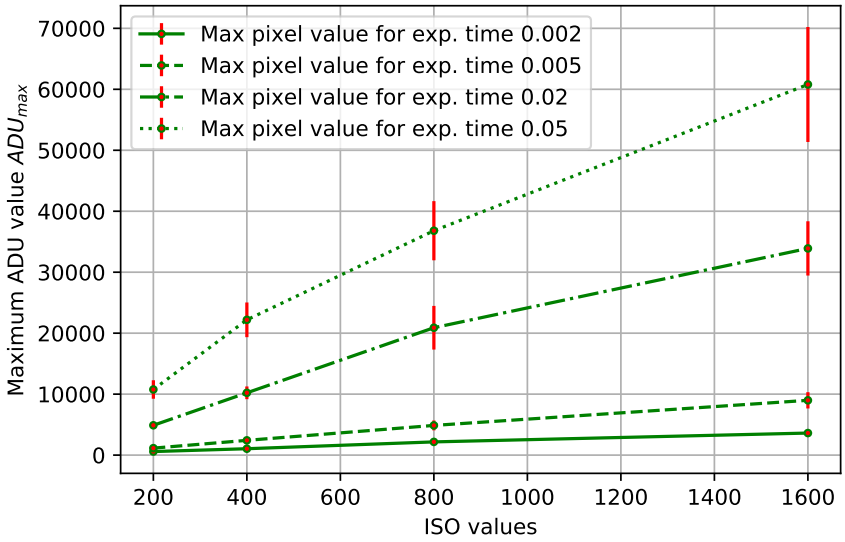

Figure 4.7.: ADU_{max} plotted against ISO for Tau Herculis.

In Fig. 4.6 ADU_{max} of the green color channel is plotted against exposure time. The most important part of the graph is the linearity for small exposure times. For each color

channel exists a diagram like Figure 4.6 that indicates an $ADU_{threshold}$ above which the linear behavior is not given anymore. Corresponding to the measurements, the threshold is $ADU_{threshold} = 20,000$.
In Fig. 4.7 the same run is used, but this time ADU_{max} is plotted against ISO for several exposure times to prove the linearity in ISO. Like before, only the data of the green color channel is represented. The presented graphs in Fig. 4.7 are rather linear for the investigated ISOs. Correspondingly, each ISO is capable of being used for the magnitude calibration. Nevertheless an ISO of 800 was chosen as a compromise between ISO and exposure time, because it proved to be the best value to observe orbital objects in LEO/MEO.
For all measurements of orbital objects and stars where the brightness should be calibrated to an apparent magnitude, ISO 800 has to be used and therefore the exposure time has to be adjusted in such a way that ADU_{max} never exceeds 20,000.

4.1.5. Maximum magnitude observable

filter letter	"color"	peak[nm]	FWHM[nm]
U	ultraviolet	365	66
B	blue	445	94
V	visual	551	88
G	green	464	128
R	red	658	138
I	infrared	806	149

Table 4.3.: Definition of the wavelengths parameters used in photometric systems.[24]

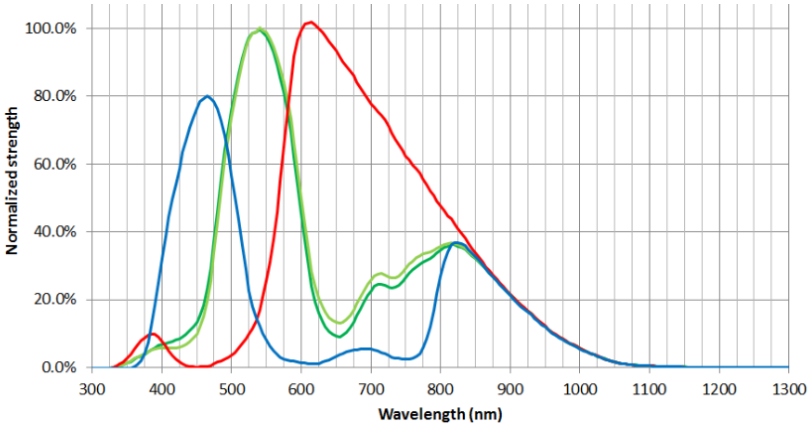

Figure 4.8.: Spectral characteristics of image sensor of ME2OF-SH.[25]

In this subsection the maximum magnitude is determined at which an orbital/celestial object can still be observed. The real brightness and thus the magnitude of an object

depends on the wavelength of the filter that was applied for the measurement. Without a system defining standards for the filter, giving magnitudes in astronomy would be meaningless. Thus, there are several common photometric systems that define pass-bands for the spectrum of wavelengths reaching from near-ultraviolet to near-infrared.[26] The astronomical database SIMBAD is used as reference for the star magnitudes.[27] The star magnitudes are given for different filter letters which are defined by the extended Johnson-Morgan photometric system. In Table 4.3 some of the filter pass-bands are characterized. However, the Bayer filters in front of the sensor pixels of the used camera have other optical properties than the defined filters. Fig. 4.8 shows the wavelength-dependent sensitivity of another CMOS sensor of Canon. The Bayer filter of the Canon camera should not differ too much from the presented sensor. Due to their similar characteristics, the green color channel is used with the magnitudes of the visible band. The utilization of the other color channels is investigated in Section 4.1.6.

For the determination several stars of different magnitude close to the zenith were

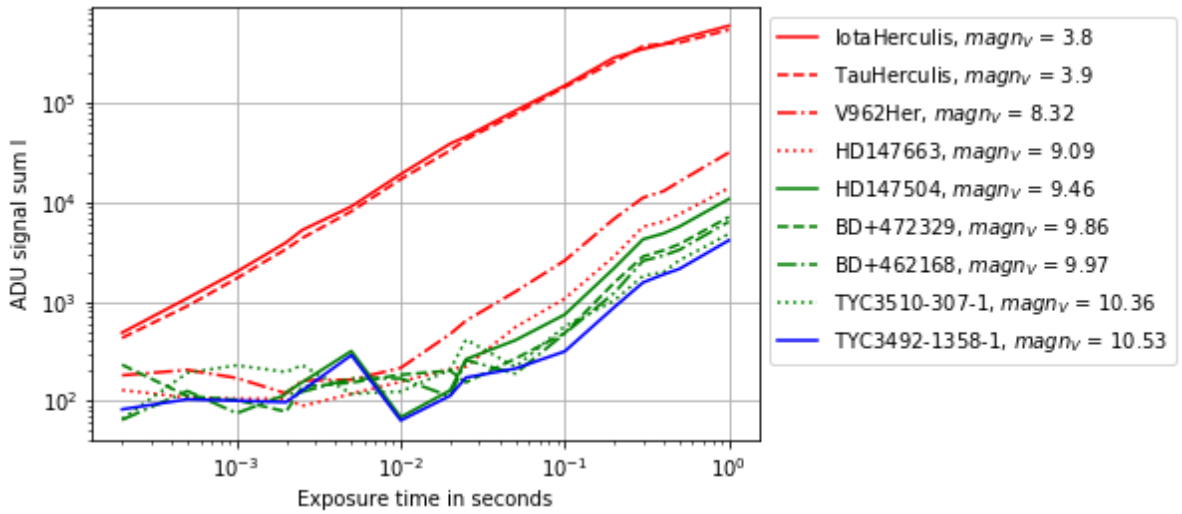

Figure 4.9.: Signal brightness of several stars plotted against exposure time for ISO 400.

observed using the routine described in Section 4.1.4. The zenith was chosen, as the attenuation due to atmospheric effects is small at this position (see air mass discussion in Section 4.1.7). In contrast to the previous section, the cumulated brightness I of the signal is of interest here. Taking the averaged I-values and plotting I against exposure time for the different stars, leads to line plots as shown in Figs. 4.9 and 4.10.
The brightness detected by LCM2 follows more or less the previously discussed linearity in exposure. Below a certain threshold that is depending on the exposure time, ISO and star magnitude, this is not true anymore. This indicates that another star or noise is mistaken for the original star which is then used to to measure I.
As the tracking is performed with ISO 800, a rough estimation of the maximum magnitude observable can be made based on Fig. 4.10. The red dash-dotted line shows that objects brighter than $magn_V = 8.32$ can be observed with exposure times of 0.005 s or

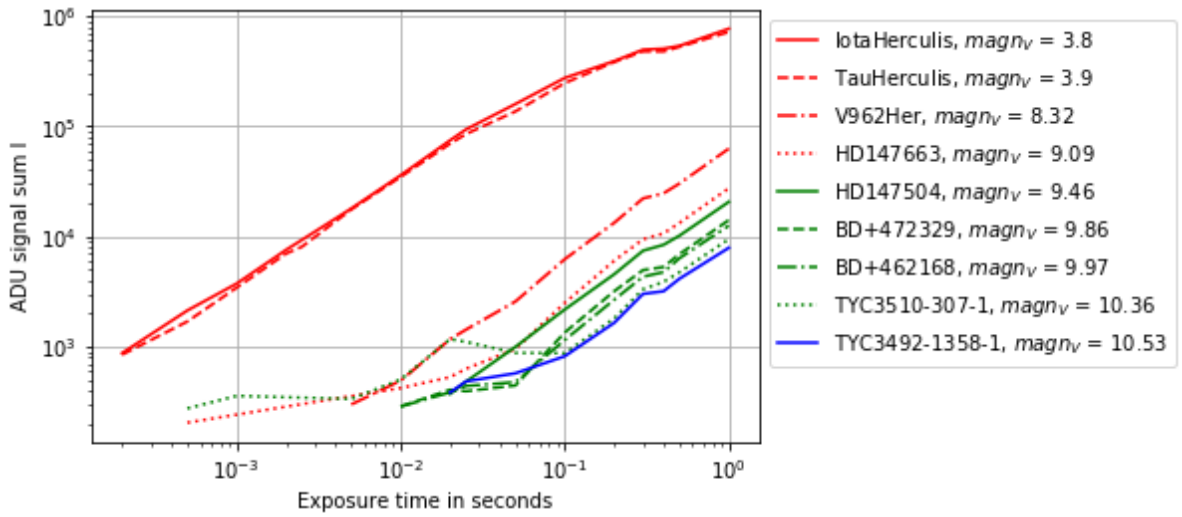

Figure 4.10.: Signal brightness of several stars plotted against exposure time for ISO 800.

higher. Objects brighter than $magn_V = 3.9$ can be observed with all exposure times, while objects brighter than $magn_V = 10.5$ need to be observed with an exposure time of more than 0.2 s. Except for the observation of objects in MEO, exposure times of more than 0.5 s are rarely used when tracking with MS-DOS.

4.1.6. Sensor color detection

As mentioned in Chapter 1, most satellites have a small number of materials that are visible from the outside like structure components made of aluminum or the solar arrays. Each of the materials possess a unique spectral reflectivity.

The ADU measurements of the two channels I_{red}, I_{blue} relative to the green channel I_{green} are investigated to test their reliability for multispectral analysis. For this purpose the relative values obtained by observing stars are used with Eqs. (4.5) and (4.6) to calculate B-V_{meas} and V-R_{meas}. Due to the measurement at different wavelengths and without a calibration of all color channels to magnitudes, the "measured color indexes" can never exactly match the real color indexes of the corresponding stars.

$$\text{B-V}_{meas} = -\frac{5}{\ln(100)} \ln\left(\frac{I_{blue}}{I_{green}}\right) \tag{4.5}$$

$$\text{V-R}_{meas} = -\frac{5}{\ln(100)} \ln\left(\frac{I_{green}}{I_{red}}\right) \tag{4.6}$$

with: I_{blue} = ADU signal of the blue color channel
I_{red} = ADU signal of the red color channel
I_{green} = ADU signal of the green color channel

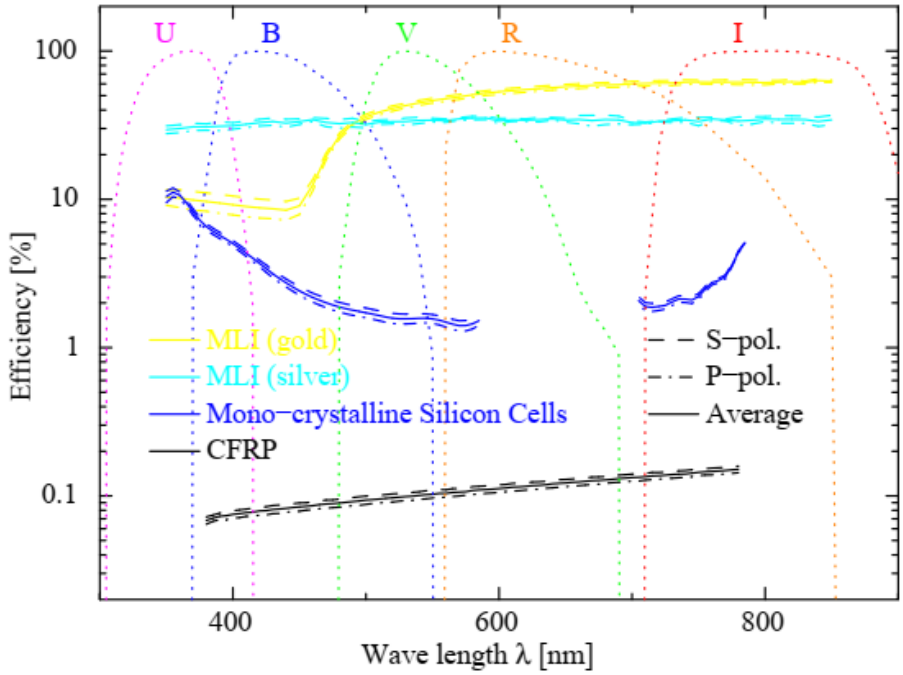

Figure 4.11.: Endo et al. Spectral measurements of satellites.[12]

As we saw in Section 4.1.3, the output of the green color channel is not very stable over time and in Eqs. (4.5) and (4.6) two of these fluctuating values are combined. Thus, to test the extent to which one can rely on the values BV_{meas} and VR_{meas} and how much they deviate from the true color index, the long-term measurement Fig. 4.4 is reused. The magnitudes of HD 159542 are $magn_B = 8.96$ and $magn_V = 7.95$ and the observed color index should be B-V = 1.01 respectively.

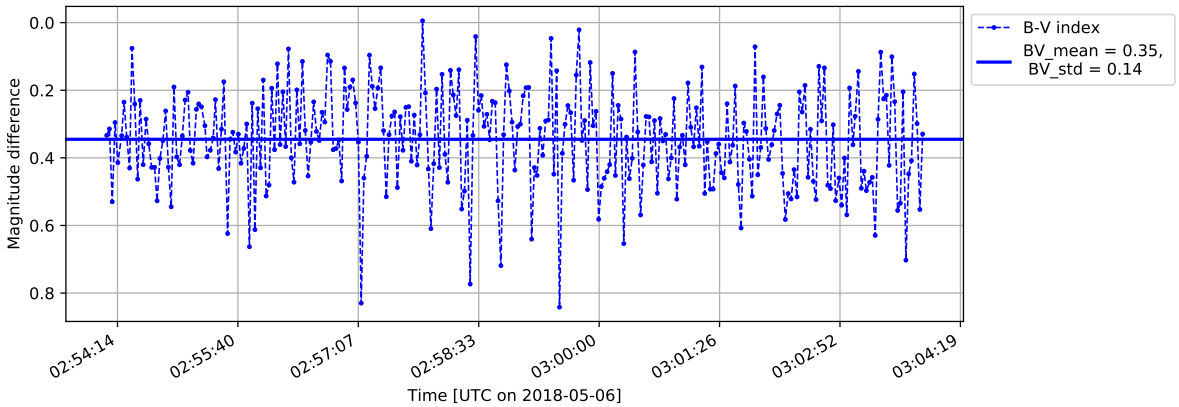

Figure 4.12.: B-V_{meas} calculated from previous observation of HD 159542 (see Fig. 4.4).

Fig. 4.12 shows that there is a clear discrepancy between the measured color index

B-V$_{meas}$ and the magnitudes stored in the database Simbad. Thus, the amplitudes of the measured color indexes are not reliable for argumentation. The terms B-V$_{meas}$ and V-R$_{meas}$ should not be confused with the scientific color indexes. Relative changes might yield some information, but as seen in Fig. 4.12, the measured color indexes feature strong fluctuations.

4.1.7. ADU-magnitude calibration

Eq. (4.7) shows the general magnitude equation. Since magnitudes are used to express intensities relative to a reference, signals transformed to magnitudes are system-independent.

$$m - m_0 = -\frac{5}{\ln(100)} \ln\left(\frac{\Phi}{\Phi_0}\right) \tag{4.7}$$

The aim of this subsection is to calibrate the cumulated brightness I obtained from the images of an orbital object and to assign an apparent magnitude to this brightness. As discussed in Section 4.1.5, the magnitude calibration is done by comparing the green channel (I_{green}) of the camera with the visible magnitude of the stars $magn_V$.
Effects that can change the brightness value I of an object independent from its magnitude, are as already mentioned in Section 4.1.4, the applied exposure time, the ISO value and the atmospheric extinction.

The Beer-Lambert law in the atmosphere (see Eq. (4.8)) is used to take the attenuation arising from scattering and transmission processes into account. Essential to the equation is the air mass, which is defined as the path length that light from an celestial

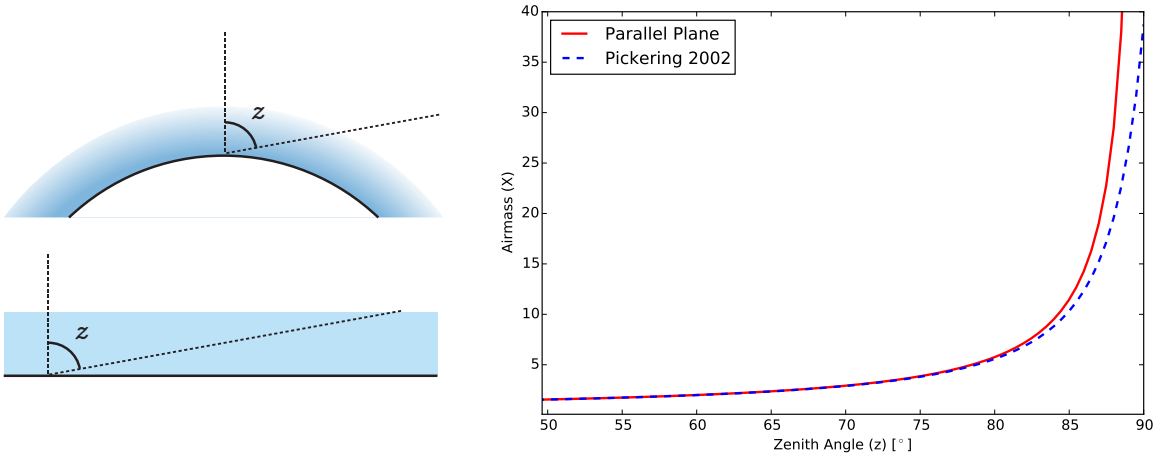

(a) Scheme of a plane-parallel atmosphere

(b) Comparison of the parallel plane model and an empirically derived model.

Figure 4.13.: Validity of the plane-parallel atmosphere model for airmass calculation. [28, p. 31]

source has to travel through the earth atmosphere. In Eq. (4.8) AIR denotes the air mass relative to the path length at the zenith.
The equation considers scattering and absorption effects of different elements in the atmosphere. For example τ_a stands for the intensity reduction caused by aerosols, w is the absorption due to water vapor, r is Rayleigh scattering from molecular oxygen and nitrogen while RS is Raman scattering. The model can be extended by adding an arbitrary number of scattering or absorption effects to the equation that take place in the atmosphere.
There are a variety of models for determining the air mass, from simple one-parameter physical models like the plane-parallel atmosphere model to complex empirical models. Due to the observation site, targets which are less than 10° above horizon are unlikely to be tracked. As can be seen in Fig. 4.13b, the deviation is negligibly small up to a zenith angle of 80°. Thus, the approximation by a plane-parallel atmosphere is applied here to calculate the relative air mass $\mathrm{AIR} = sec(z) = sec(90° - \theta)$, where z is the zenith angle and θ the altitude in the horizontal coordinate frame.

$$T = e^{-\mathrm{AIR}(\tau_a+\tau_w+\tau_r+\tau_{RS}+...)} = e^{-\frac{1}{cos(90°-\theta)}(\tau_a+\tau_w+\tau_r+\tau_{RS}+...)} \tag{4.8}$$

The factors τ_x cannot be determined individually in the experimental setup of the mobile tracking system. So for each night with calibrated light curves, the atmospheric extinction τ, which summarizes all attenuation effects, has to be determined by measuring the incoming signal of the green color channel for multiple stars at different altitudes. This results in Eq. (4.9).

$$T = e^{-\frac{\tau}{cos(90°-\theta)}} \tag{4.9}$$

Considering all three effects that can change the measured flux ϕ and the linear behavior of ISO and exposure time (see Section 4.1.4), the general equation for magnitude calculation Eq. (4.7) becomes Eq. (4.10).

$$m - m_0 = -\frac{5}{\ln(100)} \ln\left(\frac{I \cdot \frac{Exp_0}{Exp} \cdot \frac{ISO_0}{ISO} \cdot e^{(\mathrm{AIR}(\Theta)-\mathrm{AIR}_0)\tau}}{I_0}\right) \tag{4.10}$$

with:
I = measured ADU sum of the observed object
Exp = used exposure time (at I measurement)
ISO = used ISO value (at I measurement)
$\mathrm{AIR}(\Theta) = \frac{1}{cos(90°-\theta)}$

With a fictive reference star of magnitude 0 that has an ADU sum of I_0 for an exposure time of 0.01 seconds, an ISO of 800 and that is observed at the zenith position (relative air mass $\mathrm{AIR}_0 = 1$), the resulting equation is Eq. (4.11). To finally use this equation for calibrating the magnitude of an observed orbital object, the parameters τ and I_0 have to be determined by measurement.

$$m(I, Exp, ISO) = -\frac{5}{\ln(100)} \left[\ln\left(I \cdot \frac{0.01s}{Exp} \cdot \frac{800}{ISO} \cdot e^{(\mathrm{AIR}(\Theta)-1)\tau}\right) - \ln(I_0)\right] \tag{4.11}$$

For simplicity, the calibration measurements are done with ISO 800, eliminating the additional term in Eq. (4.11). Now there are two possible ways to determine the atmospheric extinction τ and the reference value I_0:
In the first method only one star is picked as calibration star. This star is observed several times at different altitudes as it moves across the night sky. Reordering Eq. (4.11) then leads to Eq. (4.12). However this method is not well-suited due to the long timespan between the measurements and the possible change in the attenuation of the atmosphere.

$$I_0 \cdot e^{-(\mathrm{AIR}(\Theta)-1)\,\tau} = I(\Theta) \cdot 10^{0.4\,m} \tag{4.12}$$

with: $I(\Theta)$ = average ADU sum of calibration star at altitude Θ
m = magnitude of calibration star

The second method is to observe various stars at different altitudes. Again, the brightness measurements are done by taking several pictures of each star at ISO 800 and exposure time in the range of 0.005 s to 0.05 s. The average of the resulting ADU sums is then used as $I(\Theta, star)$. To take the magnitude of this star into account every measured brightness $I(\Theta, star)$ is multiplied by $10^{0.4\,m(star)}$, where $m(star)$ is the magnitude of the according star. Additionally, the exposure time is normed to 0.01 s.

$$I_0 \cdot e^{-(\mathrm{AIR}(\Theta)-1)\,\tau} = I(\Theta, star) \cdot \frac{0.01s}{Exp} \cdot 10^{0.4\,m(star)} \tag{4.13}$$

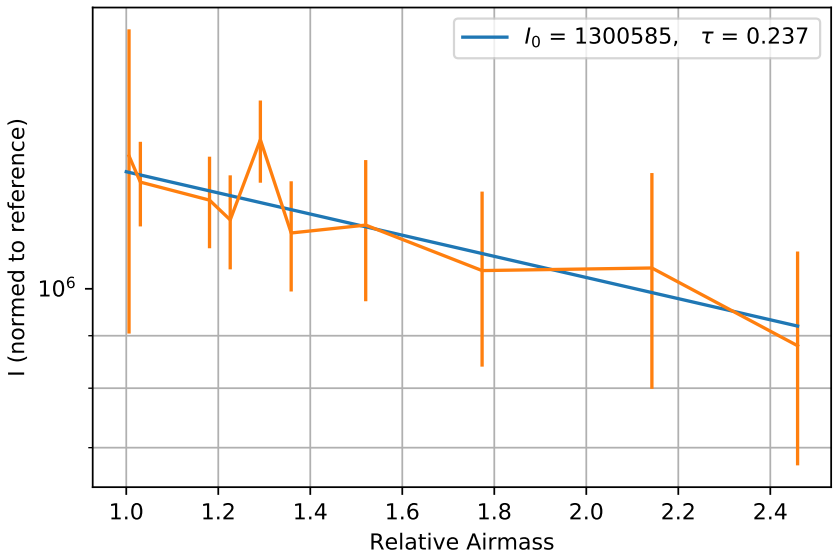

Figure 4.14.: Measured brightness of several stars at different altitudes on 2018-05-06, normed to magnitude 0., ISO 800 and exposure time 0.01 s.

Due to the semi-logarithmic formatting the exponential attenuation in Fig. 4.14 is represented by the linear fit function of Eq. (4.14).

$$I_0 \cdot e^{-x\tau} = y \tag{4.14}$$

with: $x = \mathrm{AIR}(\Theta)$ - 1
$y = I(\Theta, star) \cdot \frac{0.01s}{Exp} \cdot 10^{0.4\, m(star)}$

The resulting parameters of the calibration fit are $I_0 = 1,300,585$ and $\tau = 0.237$. Every orbital object, tracked that night (2018-05-06) can be calibrated using Eq. (4.15). As the uncertainty of each measured star is immense, the magnitudes obtained from this calibration have a large uncertainty themselves. This process has to be done for every night where the brightness of a target should be converted to apparent visible magnitudes.

$$m(I, Exp, ISO) = -\frac{5}{\ln(100)} \left[\ln\left(I \cdot \frac{0.01s}{Exp} \cdot \frac{800}{ISO} \cdot e^{(\mathrm{AIR}(\Theta)-1)*0.237} \right) - \ln(1300585) \right] \tag{4.15}$$

4.2. Auxillary optical system

The auxiliary optic system is formed by a PointGrey-camera combined with a zoom lens. The focal length of the zoom lens can be set to any value between 12.5 mm and 12.5 mm. The PointGrey-camera has a 2/3" sensor, which corresponds to a sensor size of 8.8 mm × 6.6 mm. Regarding equation 4.1 the overall FOV can be adjusted to any value between 6.7°/5.0° and 38.8°/29.6°. In contrast to the main optics, the auxiliary optical system is designed to find the calibration stars when the deviation between the telescope coordinates and the celestial coordinates is bigger than the maximum FOV of the main optics.
Therefore, the focal length is set to roughly 33 mm, setting the FOV of the auxiliary optics to 15.2°/11.4° which is well suited for detecting the right star and shifting it into the image center of the main camera.

4.3. Mount

4.3.1. Tracking accuracy

In this subsection, the tracking precision of MS-DOS will be investigated. Meant is the ability to reach the trajectory points at the predestined timestamps. As mentioned in Section 3.1.4 the trajectory points are calculated based on the latest TLE data available for the observed target. To investigate the tracking accuracy, the log-files of various runs on orbital objects are used. Each contains the calculated and the measured positions (h, δ) as well as the slewing rates of the axes. The entries are logged with a frequency of approx. 7 Hz.

Fig. 4.15 exemplifies the occurring deviation while tracking Envisat for both axes separately. The deviations are calculated by subtracting the actual and the calculated positions of the mount given in the log-files. The smaller the deviation, the more accurate is the tracking of given positions with MS-DOS.
Since the sign of the deviation is not important for the tracking accuracy, only the absolute values are used in the further course. For each run a root mean square value (RMS) can be determined, where 68,27% of the absolute deviation values are smaller than this parameter.

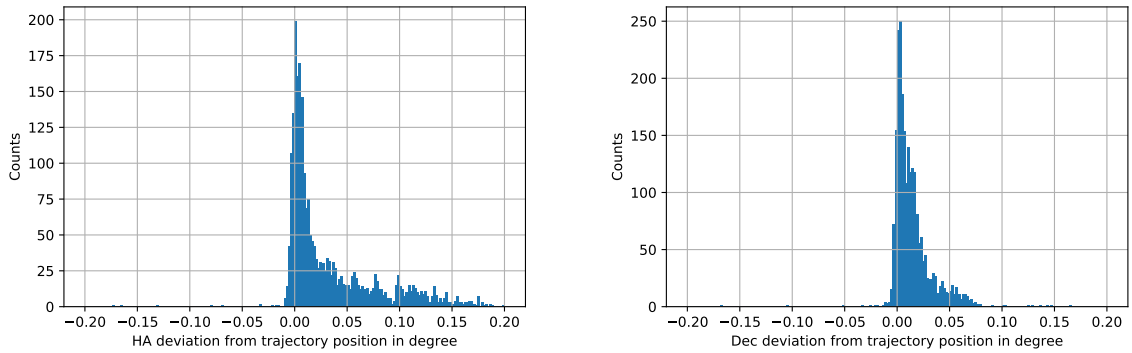

(a) Deviation in hour angle (b) Deviation in declination

Figure 4.15.: Measured deviation between mount axes position and given trajectory points.

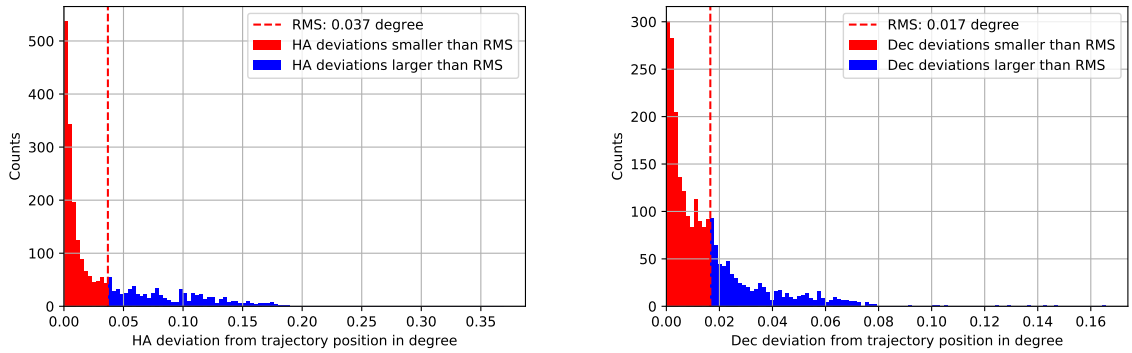

(a) Deviation in hour angle (b) Deviation in declination

Figure 4.16.: Absolute values of the deviation between mount axes position and given trajectory points.

The orbit of Envisat is almost circular with the perigee at a height of 772 km. Thus, Envisat can be considered as typical LEO object and the tracking accuracy of MS-DOS is 0.037° for the hour angle axis and 0.017° for the declination axis. Objects that are

more distant, move slower with respect to their angular velocity around Earth. The deviations for those objects are expected to be smaller than the mentioned tracking accuracy.

4.3.2. Pointing accuracy

MS-DOS is operated in conjunction with a classical pointing model for equatorial mounts. Thus, there are six geometric parameters and at least four stars are needed to fit the pointing model (see Section 3.3.1) In order to investigate the achievable pointing accuracy of MS-DOS, the pointing model is created with different sets of stars .
The first set consists of seven stars, which are equally distributed in the observation region (not containing the exclusion region Section 3.2.2). The second set contains 14 calibration stars and the last set has 23 stars. Each set contains the stars that have already been used in the former set. Using these star sets to fit the pointing model, yields three different sets of values for the six geometric parameters. For better understanding, these are referred to as PM1, PM2 and PM3 in the following.
The pointing model parameters of PM1 to PM3 are listed in Table 4.4. Striking is the major effect of the axis offsets (IH, ID), caused by the deviation between the coordinates of the mount and the real celestial coordinates.

parameters	PM1	PM2	PM3
IH	-1.322235	-1.272202	-1.211288
ID	-4.524410	-4.503607	-4.493016
NP	0.054361	-0.118534	-0.239939
CH	0.080024	0.153005	0.218046
MA	1.180728	-1.154636	-1.177894
ME	-1.101882	1.217264	1.206624

Table 4.4.: Parameters PM1 - PM3 for the classical pointing model used for MS-DOS.

Apart from the calibration stars, there is a set of six further stars (in the following called reference stars), that are used to check the quality of the pointing model parameters. The reference stars are picked from the magnitude range of 1.41 to 2.13, which makes it easy to distinguish them from other stars as they are the brightest stars in the FOV of MS-DOS. At the time of measurement, half of them were on the east side of the night sky, while the other half was distributed on the western side.
After applying the classical pointing model to MS-DOS, the reference stars are visible in the FOV. The more calibration stars are used to determine the pointing model parameters, the smaller is the expected residual deviation of the reference stars from the center of the FOV. In order to test this assumption, the remaining deviation is measured with the Closed-loop algorithm for each reference star and each set of pointing model

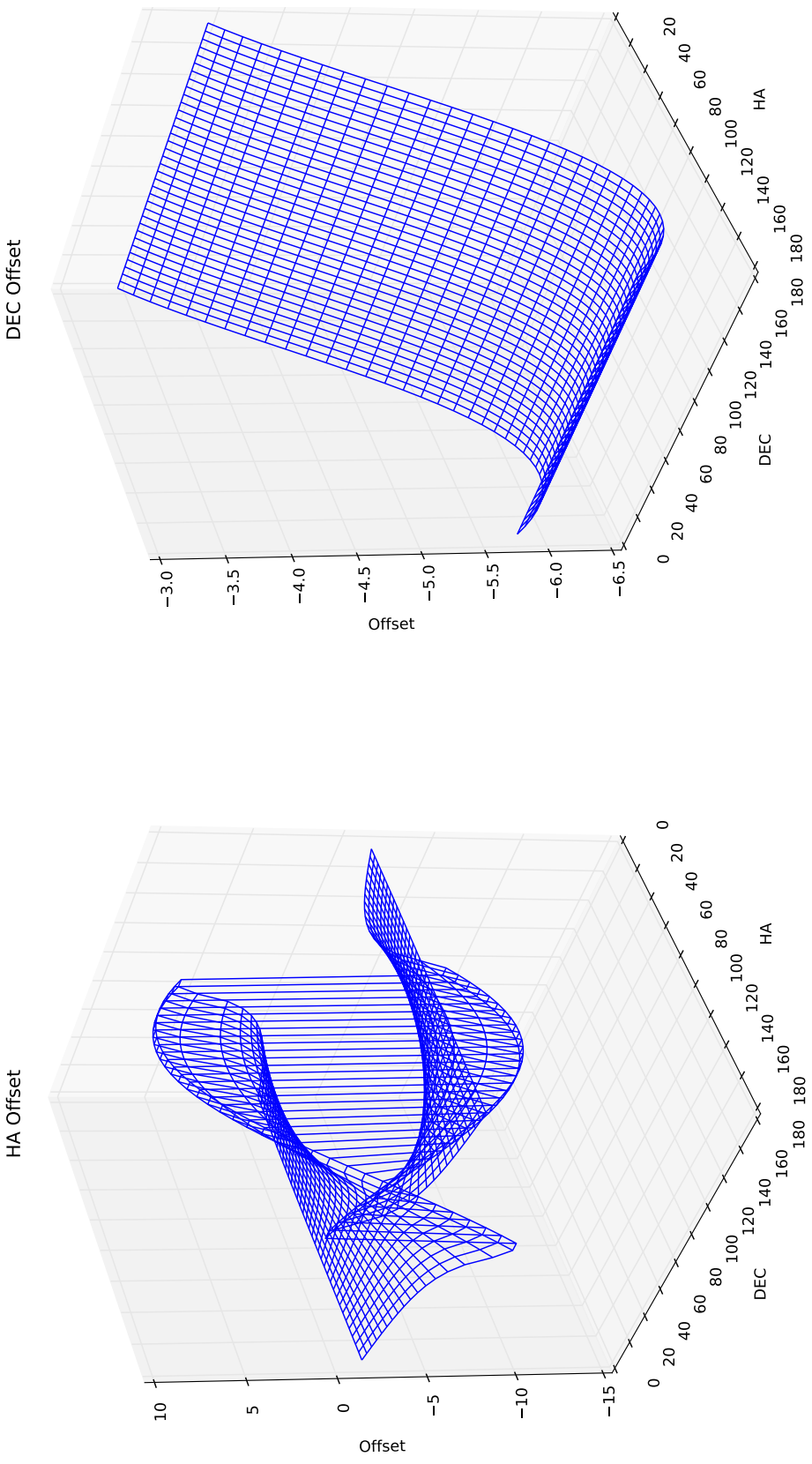

Figure 4.17.: These are the corrections in hour angle and declination that arises from the parameters PM1. Note that HA and dec at the x,y axes are mechanical coordinates with other domain of definition than celestial coordinates.

parameters (see Table 4.5). It becomes clear that the pointing accuracy is less precise than the tracking accuracy.

star \ deviation $\Delta h/\Delta\delta$	for PM1	for PM2	for PM3
Regulus	0.016/0.011	0.017/-0.050	-0.050/0.006
Mirfak	0.306/0.023	0.192/0.008	0.064/-0.063
Menkalinan	0.234/0.032	0.212/0.038	0.141/0.025
Dubhe	0.158/0.022	0.390/0.004	0.383/0.034
Alkaid	0.357/0.008	-0.101/-0.026	-0.504/0.020
Denebola	0.070/0.002	-0.082/-0.008	0.141/0.025

Table 4.5.: Deviations from each star as well as the average value using PM1, PM2 or PM3.

4.3.3. Conclusion

As mentioned above, the pointing accuracy describes the deviation between the coordinates where the telescope should be pointing and these coordinates, to which it actually points. The tracking accuracy on the other hand is the ability of the mount to follow a given trajectory. Combining the results of Sections 4.3.1 and 4.3.2 gives a rough estimation of the mounts deviation and the needed FOV when tracking an orbital object. It also shows that the pointing model is the limiting factor considering the accuracy of the mobile system for tracking satellites.
Nevertheless, the average deviation for PM2 and PM3 is almost constant. This leads to the conclusion that the accuracy of the pointing model used for MS-DOS is only slightly increasing when using 23 rather than 14 calibration stars. With regard to time efficiency, the mount will be calibrated with a set of 15 calibration stars. Correcting the internal coordinates saved in Autoslew is supposed to reduce the large deviations and might increase the pointing accuracy. For the purpose of generating light curves and with respect to the used FOV, this accuracy is sufficient for MS-DOS.

5. Results

5.1. Monochromatic lightcurves

5.1.1. General

The preceding chapters describe the procedure for observing orbital objects. The recorded image series are now analyzed with the LCM2 and the obtained light curves are evaluated with regard to the occurring brightness fluctuations.
For the further discussion, Fig. 5.1 is used to introduce some important parameters. R is the distance between target and observer. The phase angle is denoted as β. The zenith angle (see Section 4.1.7, not shown here) is complementary to the target's altitude *alt* in the horizontal observer system.

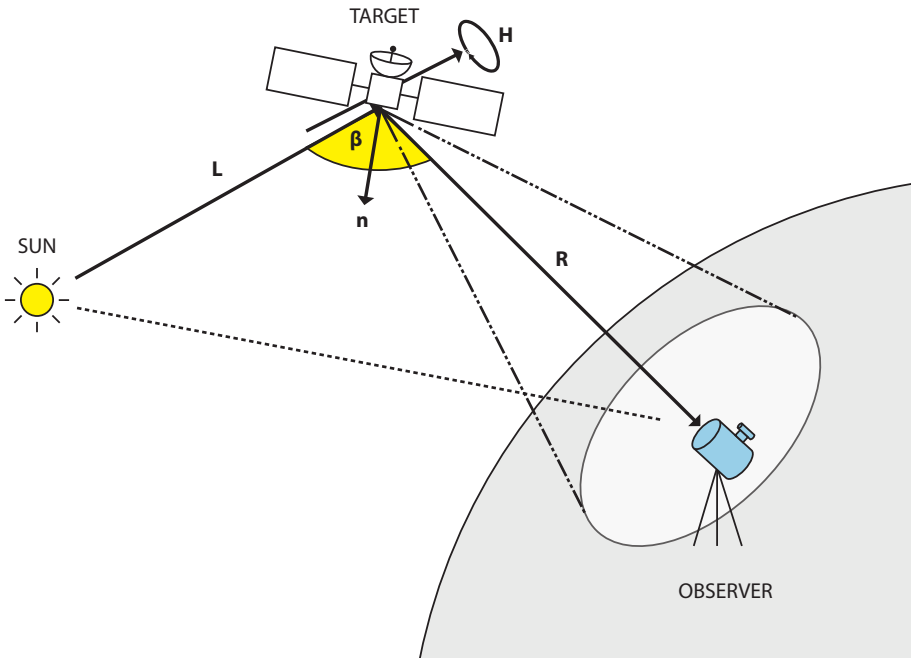

Figure 5.1.: Schematic drawing of the sun-target-observer system. [28, p. 13]

The light curves in Fig. 5.2 are created with the software tool "Raxus Prime 2.1" by Ewan Schafer [28] and are used to illustrate some general effects related to light curves. A homogeneous sphere is simulated in the orbit of the international space station (ISS) (circular orbit at a height of roughly 400 km above Earth's surface).

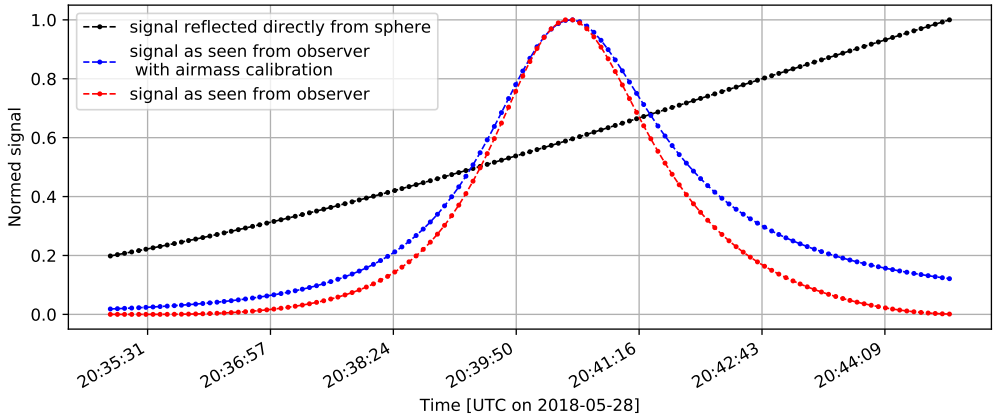

Figure 5.2.: Simulated sphere on ISS orbit for pass on 2018-05-28 using Raxus Prime 2.1.[28]

Apart from the rotation of an object there are other influencing factors that change the measured brightness of an object over time. Although the illuminated surface of the sphere always remains constant, the strength of the signal that is reflected in the direction of the observer (black graph in Fig. 5.2) increases as the phase angle β gets smaller. Additionally, the distance R and the zenith angle influence the observer's received signal:
First, the distance R decreases steadily until 20:40:30 UTC. Due to its R^{-2} dependency, the brightness increases accordingly. Although the sphere moves away from the sun at the same time, the relative increase in L is insignificant. [28, p. 30 ff.]
Second, the zenith angle changes during the pass and reaches its minimum value at 20:40:30 UTC. As already described in Section 4.1.7, the transmittance during passage through the atmosphere depends strongly on the zenith angle. The smaller the zenith angle, the lower the attenuation in the atmosphere and the stronger the signal of the target.
The red curve in Fig. 5.2 illustrates the signal of the simulated sphere as received by an observer on the ground. As result of the magnitude calibration, the described influence of the atmosphere is eliminated. The blue light curve is simulated by neglecting the atmosphere. For real measurements the individual measured values I_{green} are converted to apparent magnitudes $magn_V$ by using Eq. (4.15) and the two parameters I_0 and τ.
One of the most interesting topics in the analysis of light curves is the determination of the rotation frequency based on the recorded data. To determine the period of a light curve, the phase dispersion minimization (PDM) is used here. [28, p. 39 ff.] A given range for the possible period time is scanned in a user defined step size. All PDM analysis are done with 0.1 s. A repetitive pattern in the measured light curve is a fundamental requirement for the determination of the rotation period. To check the outcome, Phase Folding (PF) of the light curve with the best suitable period is performed for each PDM analysis.
In summary, one can say that the brightness variations of a light curve are determined

by the distance R, the zenith angle, the phase angle β, the rotation and the surface properties of the target. As discussed in Section 4.1.3, these variations are superimposed by the fluctuations due to the atmosphere.

5.1.2. LEO objects

The original data obtained by the LCM2 module look like Fig. 5.4. Plotted is the object's signal brightness as ADU sum I_{green} against the observation time. As mentioned in Section 4.1.5 the green color channel is used as it corresponds to the passband characteristic of the visible magnitude $magn_V$.
Shown in Fig. 5.3 is the Canadian satellite ISIS-1, which was used to study the ionosphere of the Earth and was launched in 1969. ISIS was operational till 1990 and is specified as LEO object, with the perigee at 575 km and the apogee at 3525 km. The observation of roughly 6 minutes is performed with a frame-rate of 0.2 Hz. The images are all taken with an exposure time of 1 s and ISO 12800.

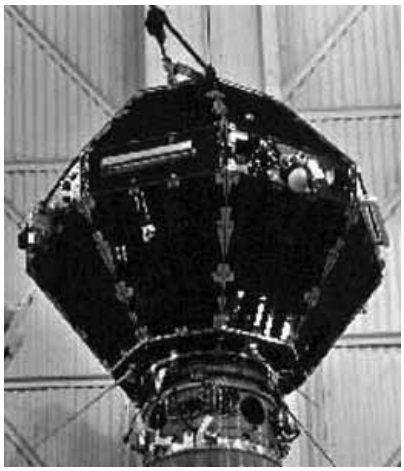

Figure 5.3.: Image of ISIS-1.[29]

In the first 4 minutes the signal of the satellite is extremely weak. Starting at 23:37:30 UTC, the intensity of the signal grew, reaching a level where it is clearly distinguishable from the image background. Shortly after the first peak at 23:38:40 UTC, a second peak appears at 23:39:10 UTC. Note, that this observation was done with an inappropriate ISO which lead to saturation and overexposure of the pixels in the center of the signal. Nevertheless, the peaks can be used for qualitative discussion.

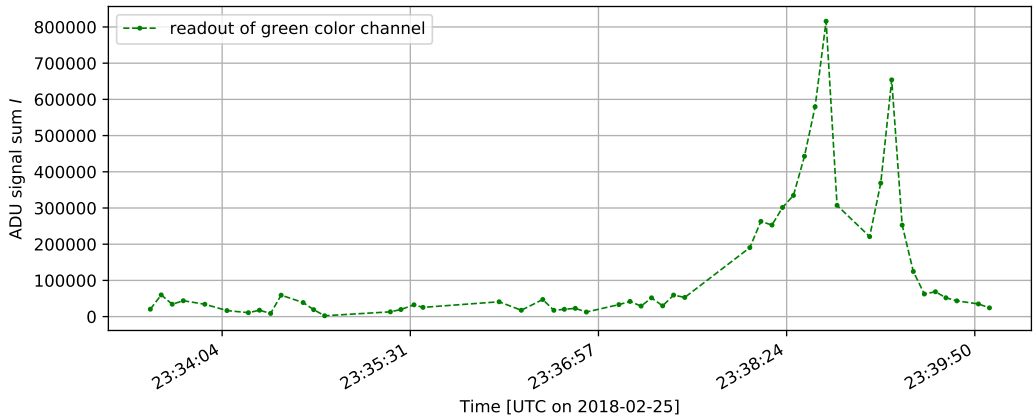

Figure 5.4.: Uncalibrated light curve of ISIS 1, observed on 2018-02-25.

Due to their highly concentrated and directed intensity characteristic, specular reflec-

tions are visible as sharp peaks in light curves. Based on the geometry of ISIS-1, the peaks in Fig. 5.4 might belong to specular reflections from two of the 16 identical sides of the satellite.
In contrast to ISIS-1, which is uncontrolled and has an unknown rotation frequency, the attitude of international space station (ISS) is controlled. Due to shielding, observation and other mission-related reasons, the ISS maintains an LVLH (local vertical, local horizontal) attitude. This means that the space station's body axis is aligned with its orbit coordinate frame and only one side is seen from an observer on Earth. To maintain this position, the pitch of the ISS is roughly four degrees per minute corresponding to 360° per orbit revolution. Due to the large size of the space station, a strong signal is expected. As the solar arrays always face the sun and the single modules are small compared to the overall size of the space station, the light curve of an ISS pass should not contain any sharp peaks like the above presented light curve of ISIS-1. In fact, the results of the ISS observation on 2018-04-07 (Fig. 5.5) are compliant to this assumption.

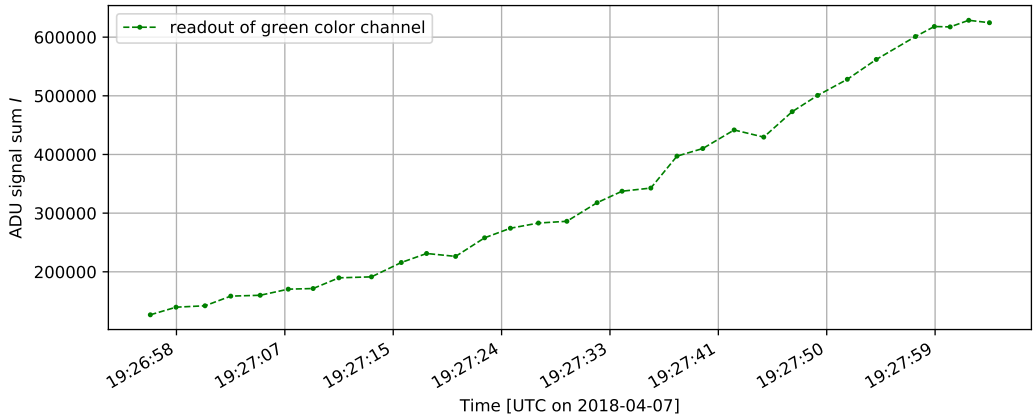

Figure 5.5.: Uncalibrated light curve of space-station ISS, observed on 2018-04-07.

From the observation start till 19:28:00 UTC the light curve shows a steady increase in intensity. In the observed time the ISS rotates only by 4°. Thus, to explain the brightness change the movement of the ISS has to be taken into account as well.
The distance between observation location and ISS decreased till it passed the point of closest approximation (on the North-South line) at 19:27:58 UTC. Passing this line, the target's pier side change and OOOS is programmed to perform a pier flip subsequently. In the last two captured images the ISS is moving away from the center of field of view. As the observation is stopped due to the pier flip, the ISS light curve can be compared to the first half of the simulated light curve (red curve, Fig. 5.2).
Note, that the observation was done in the evening. As the ISS moves to the east and pitches slowly, the phase angle decreases causing more light to be scattered back to the observer. In conclusion all the effects, the distance change R (major), the zenith angle and the rotation contribute to the observed light curve.

Terra is a NASA Observation Mission satellite orbiting the Earth in a sun-synchronous and almost circular orbit at approximately 700 km altitude. The light curve of the satellite Terra on 2018-05-06, shown in Fig. 5.6, is a typical example for observations of LEO objects as most of them have polar orbits. The satellites altitude in the horizontal observer system changed from 33.1° at the beginning to 36.4° at its maximum elevation to 11.6° at the end of the observation.
As stated above in Section 5.1.1, the magnitude calibration takes the additional atmospheric attenuation into account that occurs when an observation target moves to lower altitudes. For a LEO object that covers a wide range of different altitudes during a pass the calibration can have a significant effect on the appearance of the light curve. The pass of Terra in the observer's reference frame can be seen in the polar plot of Fig. 5.6.
The calibration parameters for that observation night are $I_0 = 1300585$ and $\tau = 0.237$.

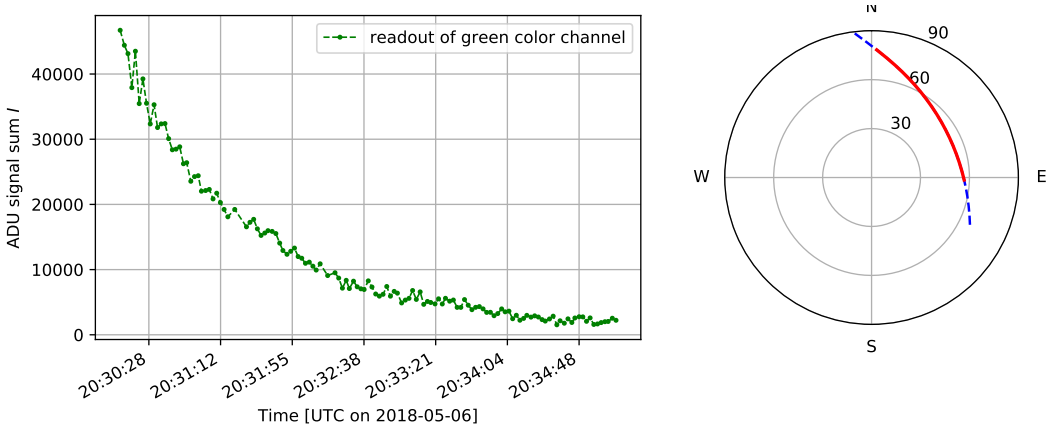

Figure 5.6.: Left: Uncalibrated light curve of Terra. Observation on 2018-05-06. Right: Trajectory of Terra with zenith angle and cardinal points. The red part indicates the observed trajectory.

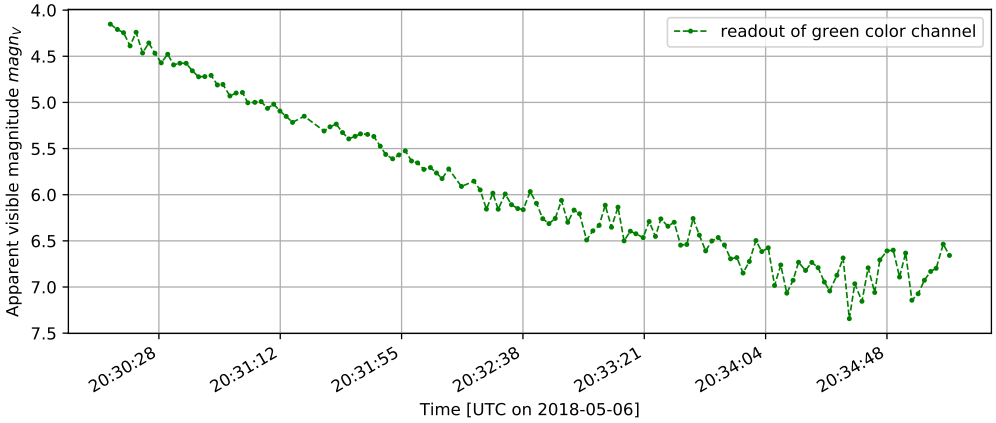

Figure 5.7.: Calibrated light curve of Terra. Observation on 2018-05-06.

The distance R during the observation is plotted in Fig. 5.8. Applying a correction based

on the R^{-2} intensity decrease as well as the magnitude calibration to the recorded signal, yields that the atmosphere and the distance between target and observer are not the main causes for the observed intensity decrease. The (air mass) calibrated light curve is shown in Fig. 5.7, proving that the phase angle has a major effect on the recorded signal intensity.

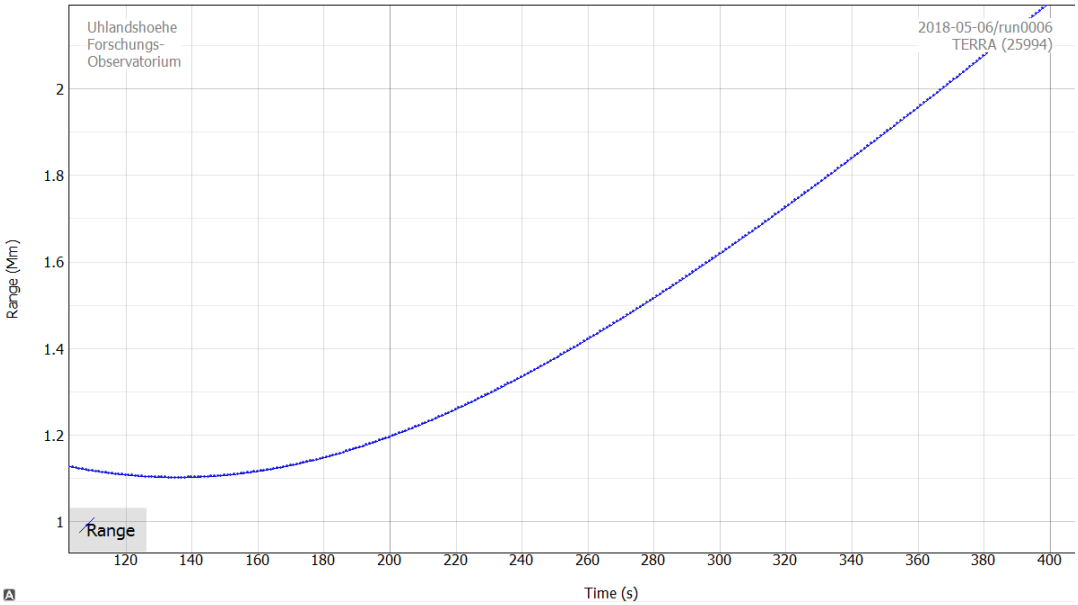

Figure 5.8.: Distance R of Terra during the observation on 2018-05-06 (20:30 - 20:35 UTC).

5.1.3. MEO objects

The ideal case to observe the brightness change of an orbital object caused by its rotation would be a fixed sun-target-observer system (see Fig. 5.1), where the angle β does not change and the distances R and L are constant. An approximation of the ideal case should be given for rotation periods far smaller than the objects orbit period. On the other hand, the rotation period needs to be large compared to the exposure time and the inverse frame-rate to resolve the brightness changes due to the rotation.
As shown in Fig. 5.5 the rotation period of objects that rotate slowly with respect to their orbit revolution period can not be determined by passive optical observations. In contrast to LEO objects, objects in MEO have a far smaller orbital angular velocity and thus they are visible for several hours per pass.
The downside of taking these objects as light curve targets is their great distance to the earth. The compensation of the lower brightness caused by the greater distance, requires either a telescope with a bigger aperture or longer exposure times for each image. In the case of MS-DOS, the exposure time had to be increased to 5 s which leads to a decrease in the time resolution of the light curve.
First, the measurement of Navstar 53 is presented. The Navstar satellites form the basis

of the US Global Positioning Navigation Satellite System (NAVSTAR-GPS). The system is commonly known under the name "GPS". Navstar 53 was launched in December 2003, has a mass of about 2 tons and a size of 152 cm × 193 cm × 191 cm. The satellite is on a circular orbit at 20.200 km altitude and is still operational.

The light curve of Navstar 53 in Fig. 5.9 shows a very low signal strength despite the

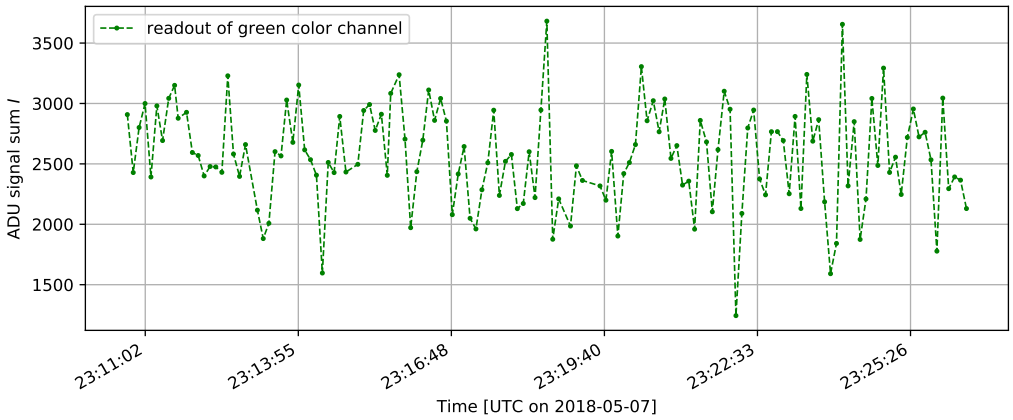

Figure 5.9.: Uncalibrated light curve of navigation satellite Navstar 53, observed on 2018-05-07.

exposure time of 5 seconds. An estimate of the magnitudes provides results between $magn_V = 12$ and $magn_V = 14$ (if taken approx. $I_0 = 1,310^6$). This measurement marks the maximum magnitude limit for the observation of objects in MEO using MS-DOS. If the signal strength is lower, the target would no longer be distinguishable from the image background.

As the satellite is still operational, it is not expected to observe strong brightness variations and a determination of the rotation time should be not possible here.

In contrast to Navstar 53, the defunct satellite Cosmos-2375 does not maintain a spe-

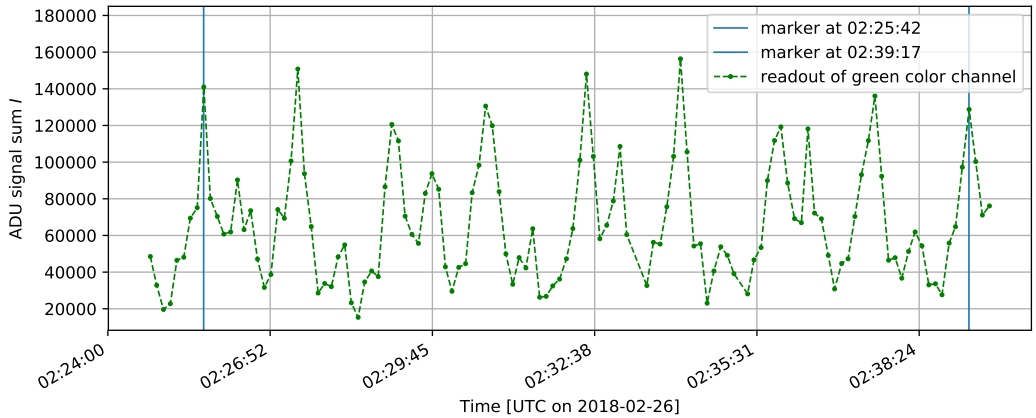

Figure 5.10.: Uncalibrated light curve of Cosmos-2375. Observation on 2018-02-26 with ISO 12800.

cific attitude. Cosmos-2375 was launched in October 2000 and belonged to the Russian satellite navigation system GLONASS. The system consists of 21 operational satellites which are located on circular orbits at an altitude of roughly 19.000 km above Earth's surface.

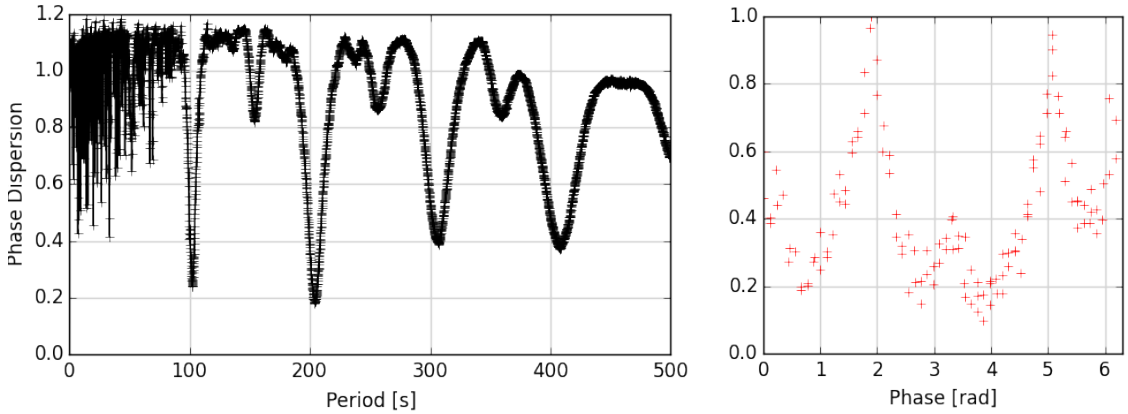

(a) Phase Dispersion Minimisation analysis

(b) PF with 203.7 s

Figure 5.11.: PDM applied on the data set of Cosmos-2375, observed on 2018-02-26. The most suitable period time is 203.7 s ± 7.1 s.

The observation results of Cosmos-2375 on 2018-02-26 (shown in Fig. 5.10) reveal a certain pattern. The pattern consists of a double peak, followed by a higher and a smaller peak. Evaluating the light curve with regard to recurring peaks give a rough estimate for the satellites rotation period. Starting at the fist marker the brightness pattern is represented four times in the next 13:35 minutes, leading to a rotation period of roughly 3 minutes and 24 seconds. Using the aforementioned PDM analysis in Raxus Prime 2.1, the rotation period is evaluated to 203.7 s ± 7.1 s. The uncertainty is half of FWHM of the corresponding peak in Fig. 5.11.

5.1.4. Lightcurves as fingerprints?

After highlighting all the different elements that can be found in a light curve, it has to be discussed if it is possible to assign unique light curve elements to orbital objects. If this is the case then it has to be discussed whether it is possible to distinguish orbital objects solely based on their light curves. (anders formulieren)
A light curve from Cosmos-2375 was already shown above (see Fig. 5.10), proving that there is a certain pattern in the brightness changes. Nevertheless, this pattern changed gradually during the observation time, indicating that it might not occur in a light curve taken at another date.

Fig. 5.12 shows another observation of Cosmos-2375, this time taken on 2018-03-15.

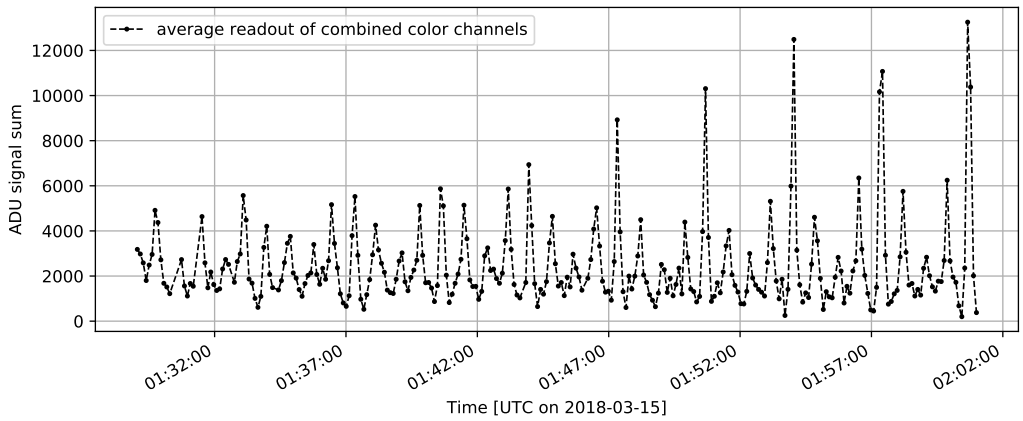

Figure 5.12.: Uncalibrated light curve of Cosmos-2375, observed on 2018-03-15 with ISO 800.

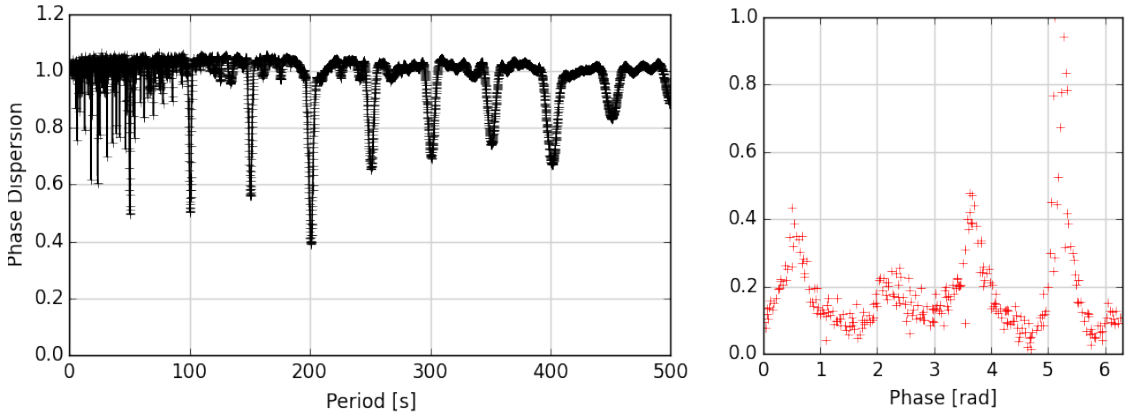

(a) Phase Dispersion Minimisation analysis

(b) PF with 200.8 s

Figure 5.13.: PDM applied on the data set of Cosmos-2375, observed on 2018-03-14. The most suitable period time is $200.8\,\mathrm{s} \pm 2.1\,\mathrm{s}$.

Unfortunately, the software failed in this night and, instead of the desired 3D colour array, a 2D array with the mean of all three color channels was saved in the FITS images (see Section 3.4). The result of the PDM evaluation is a rotation period of $200.8\,\mathrm{s} \pm 2.1\,\mathrm{s}$. Comparing the period means and uncertainties yields that the measurements are compatible to each other.
Apart from the rotation frequency there are other light curve elements that both observations have in common. The pattern in the light curves recurs after four peaks, although the intensity of the individual peaks changes over time. The noticeable peak in the later observation on 2018-03-15, might occur from an specular reflection as it increases with time.
Although the measured brightnesses of both light curves can not be converted to magnitudes, the amplitudes (ADU signal sum I) can still be compared in some way. The

amplitude of the green color channel lies in between the other color channels. Under consideration of the different ISO values, the amplitudes of both light curves are in the same order of magnitude. (Note, that the orbit of Cosmos-2375 is approx. circular.)
Attached is a measurement of Cosmos-2375 on 2018-05-26 taken with UFO (Fig. A.1). Again, the pattern consisting of four peaks can be recognized. The evaluation of the light curve to 211.5 s ± 7 s shows that the rotation period of Cosmos-2375 has slightly changed over the last two months (see Fig. A.2).
Although the obtained light curves look similar in some way, this investigation shows primarily that, apart from a repetitive pattern in the observed light curves and the rotation period of the object, further indicators are needed to assign an observed light curve to a certain orbital object out of almost 20,000 present in space.

5.2. Color index on orbital objects

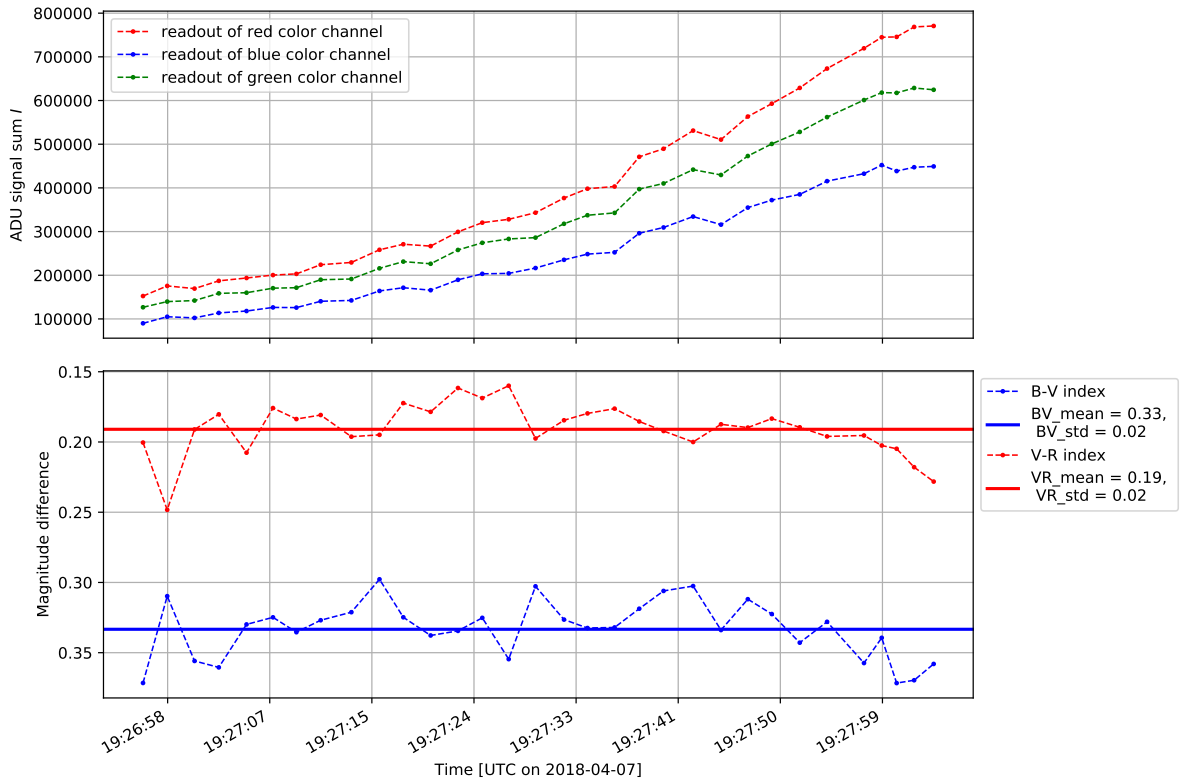

Figure 5.14.: Multispectral evaluation of ISS pass on 2018-04-07. Uncalibrated light curves of all three color channels and underneath the resulting time-resolved color indexes B-V_{meas} and V-R_{meas}.

MS-DOS takes multispectral measurements in the process of tracking orbital objects. In addition to the measurements of the green color channel of the camera, there are also time-resolved values for the red and blue color channel. Eqs. (4.5) and (4.6) convert the

Object			Measurements	
Name	Date	UTC	B-V_{meas} index	V-R_{meas} index
ISS	2018-04-07	19:27-19:28	0.33 ± 0.02	0.19 ± 0.02
H-2A R/B	2018-05-06	19:12-19:16	0.51 ± 0.32	0.10 ± 0.40
Interkosmos 24	2018-05-06	20:37-20:41	0.45 ± 0.19	0.19 ± 0.13
SL-16 R/B (25407)	2018-05-06	21:49-21:54	0.51 ± 0.15	0.31 ± 0.14
Cosmos-482 Descend	2018-05-07	21:27-21:41	0.25 ± 0.06	0.20 ± 0.08
Sert 2	2018-05-07	22:03-22:09	0.53 ± 0.29	0.17 ± 0.30
Terra	2018-05-07	22:51-22:54	0.80 ± 0.24	0.43 ± 0.12

Table 5.1.: Mean and standard deviation for several observed targets. Measured values are obtained from the different color channels.

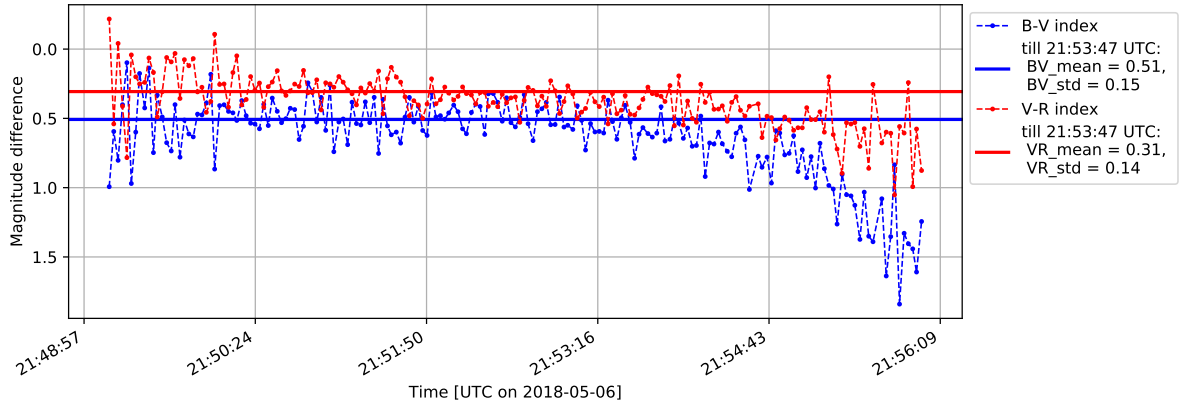

Figure 5.15.: Color indexes B-V_{meas} and V-R_{meas} for SL-16 R/B (Norad ID: 25407), observed on 2018-05-06. The rocket body's pass was tracked to approx. 3° above horizon.

measurements to time-resolved ratios of the channels.
For the discussion of the obtained results, the previously presented observation of the ISS on 2018-04-07 was chosen. As the ISS rotates slowly compared to the observation duration, the color indexes of the light reflected from the space-station are expected to be rather stable. In Fig. 5.14 the measured brightness values and the resulting ratios are presented.
Compared to the previous measurements of a star shown in Section 4.1.6, the ISS shows significantly less variations in the light curves. The quality of the MS-DOS light curve is still insufficient for an evaluation of the individual measured values. With a suitable characterization of the color channels and under consideration of atmospheric effects, it might be possible to evaluate the obtained mean values and give a rough estimate of the satellites materials. But this topic is clearly beyond the scope of this master thesis.

Table 5.1 contains a selection of observed color index values for different orbital objects. As shown in Table 5.1, most of the mean values have large uncertainties and further improvements to MS-DOS need to be done.
The measurement of SL-16 R/B (Norad ID: 25407), which is shown in Fig. 5.15 should be pointed out. The rocket body is observed as it passes from 13° altitude in the north to 3° above the eastern horizon. Striking is the strong increase in air mass for small angles above the horizon. Smaller wavelengths are attenuated more in the atmosphere, which is visible in the measured color index. Note, that all measured color indexes which are shown in this section are only time-resolved ratios of the color channels and should not be mistaken for astronomical color indexes.
The second point to highlight is that the noise of the measured color indexes is correlated with the amplitude of the target's signal. The weaker the input signal, the more intense are the observed variations. This can be seen in Fig. 5.19 on page 64 as the noise of the color indexes increases steadily with the decreasing signal.

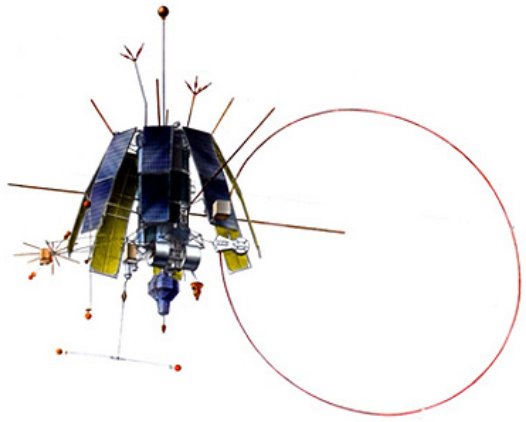

Figure 5.16.: Artists illustration of Interkosmos 24 [30]

With regard to multispectral analysis, the main interest of this thesis was to observe light curves with dominant peaks.[31] These peaks would indicate that most of the signal was emitted by a particular part of a satellite, such as a large solar array or a large reflective surface. Due to the fact that different surfaces have different spectral emission and reflection properties, the observed color index of the object might change for the peak.
For illustration, the observation of the satellite Interkosmos 24 (Fig. 5.16) on 2018-05-06 is used. The signal of Interkosmos 24 becomes steadily weaker in the course of the measurement. At the end of the light curve, the brightness increases sharply and then returns to the normal course. Contrary to the assumption, no major difference can be recognized in the course of the color indexes as the peak occurs. Comparing Fig. 5.17 with Fig. 5.14 shows how strongly the fluctuations of the color index depend on the uniformity of the measured light curves. At the current resolution of the light curves, all possible elements disappear in the noise of the measured values.
Finally, the according measurement of Cosmos-2375 will be presented. In contrast to the other examples, systematic abnormalities occur in Fig. 5.18. There is a little tip in the signal of the red color channel at the marked positions, which is not visible in the other color channels.

This effect might be caused by an element on the satellite that has other material properties than the rest of the satellite and reflects more in the long wavelength range of the optical spectrum. Unfortunately, until now there are no other multispectral mea-

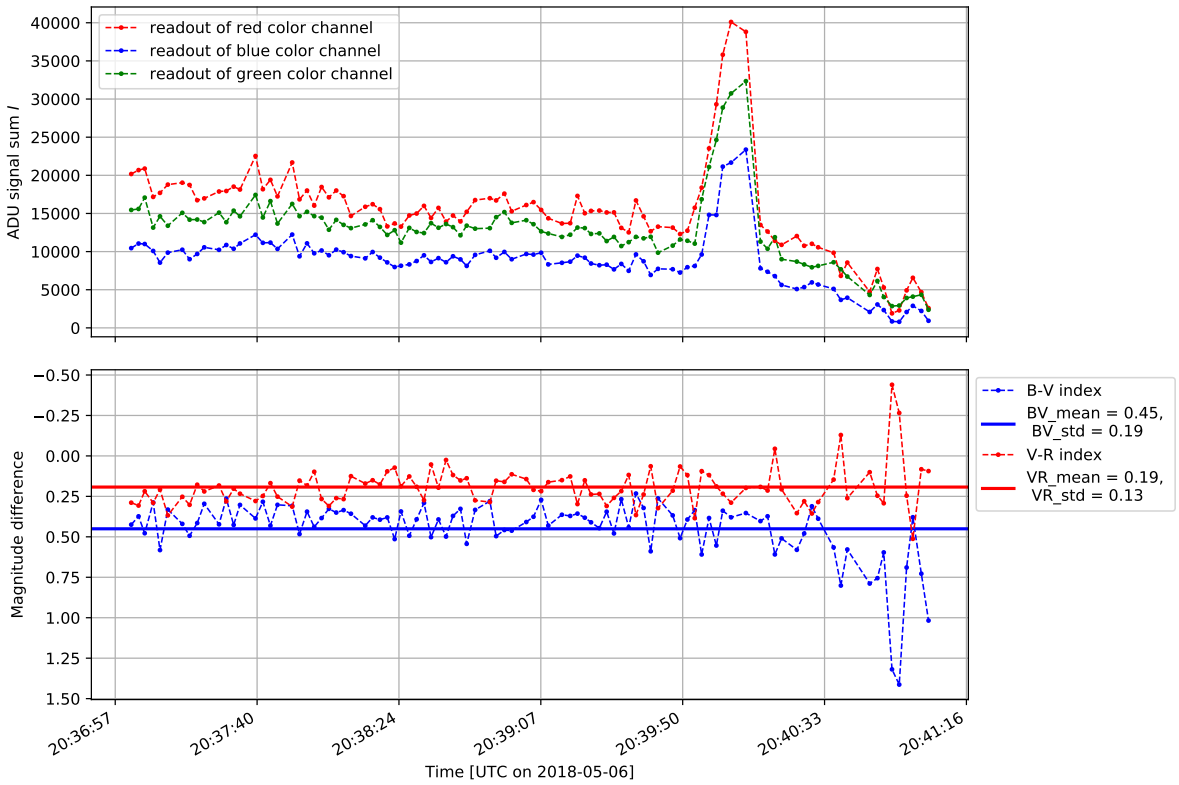

Figure 5.17.: Multispectral evaluation of Interkosmos 24 pass on 2018-04-07. Uncalibrated light curves of all three color channels and underneath the resulting time-resolved color indexes B-V_{meas} and V-R_{meas}.

surements of Cosmos-2375 to test this theory. In the end, this is solely a guess that has to be proven or refuted in further observations.

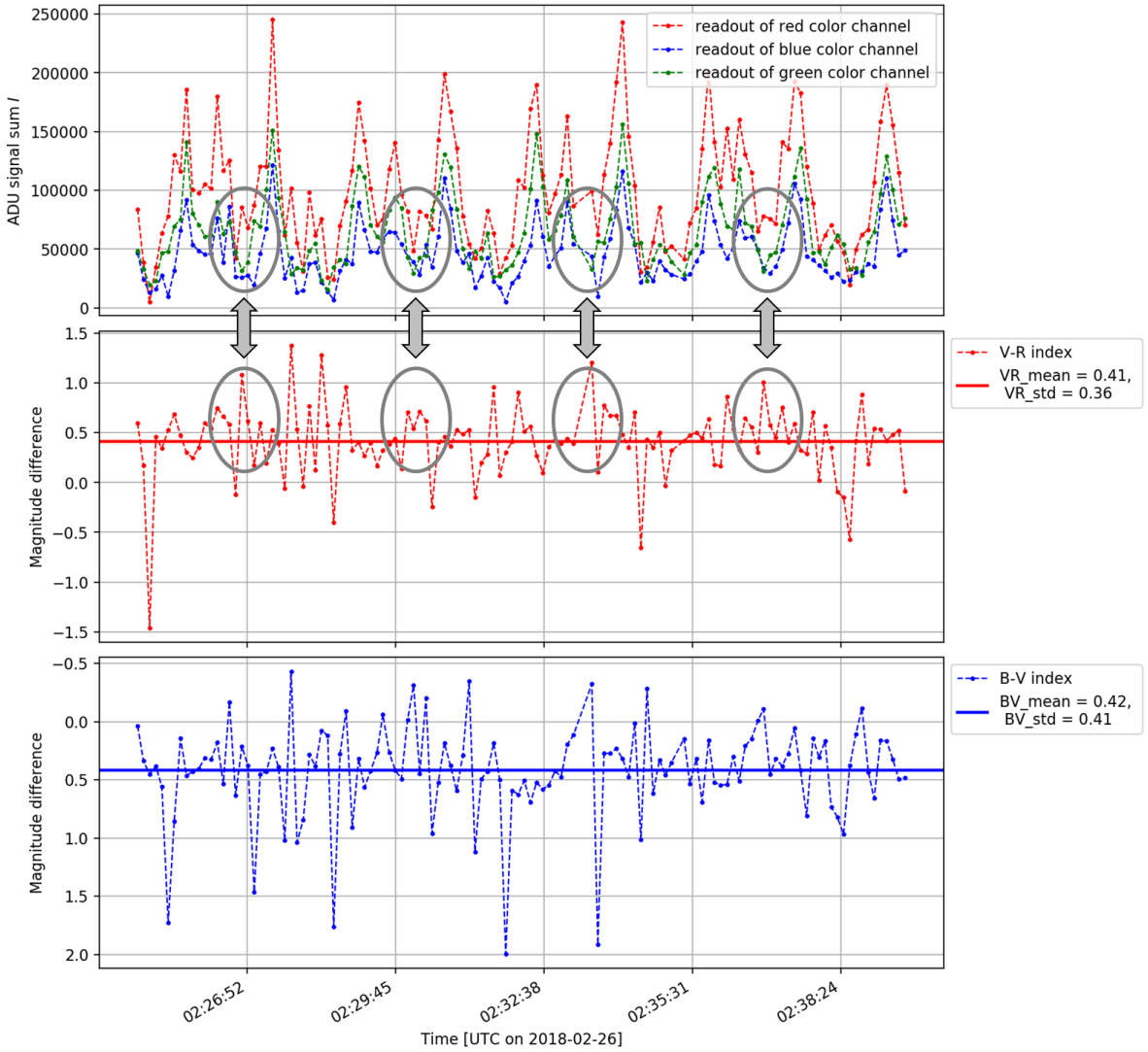

Figure 5.18.: Multispectral evaluation of Cosmos-2375 pass on 2018-02-25. Uncalibrated light curves of all three color channels and underneath the resulting time-resolved color indexes B-V_{meas} and V-R_{meas}.

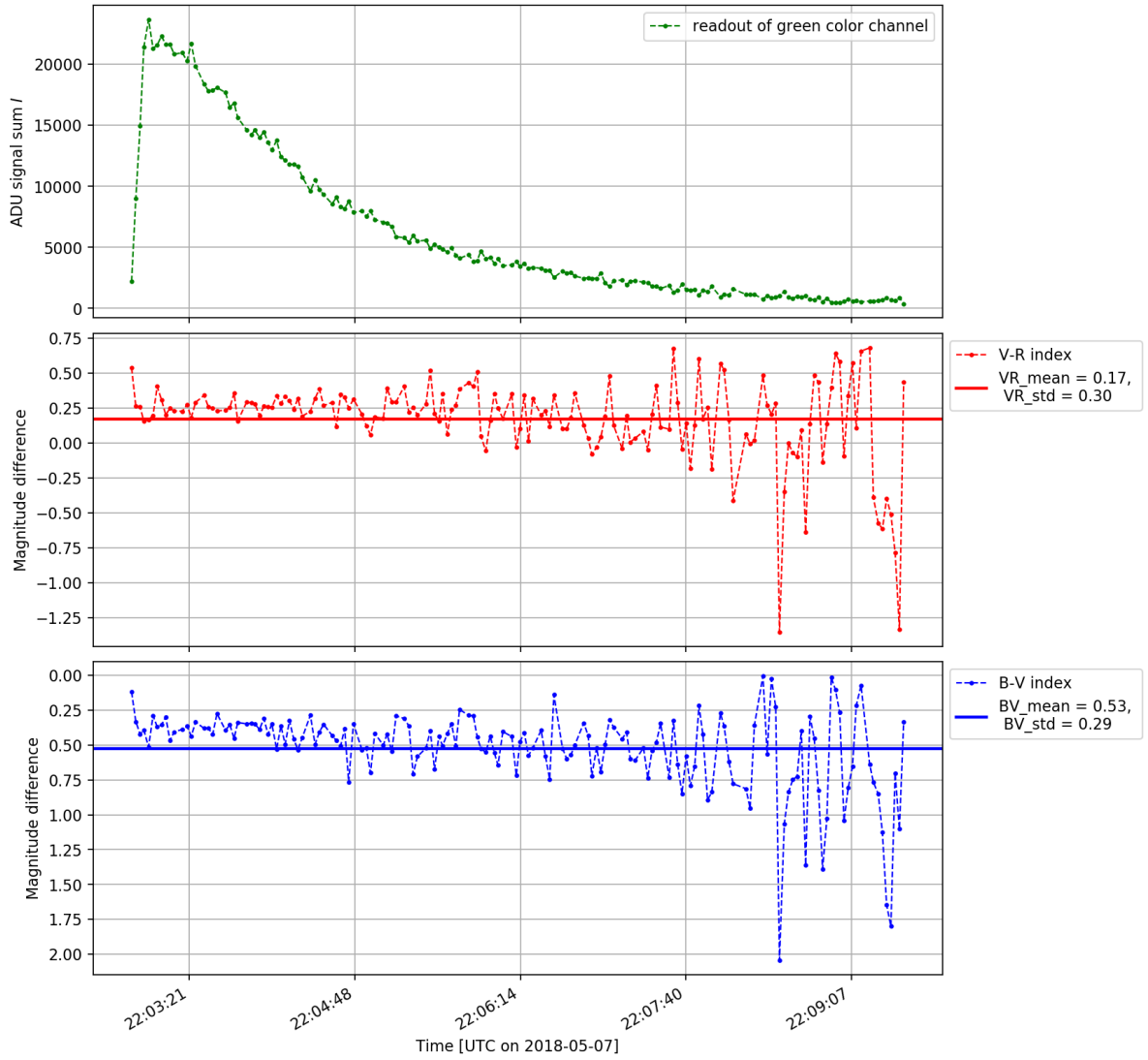

Figure 5.19.: Multispectral evaluation of Sert-2 pass on 2018-05-07. Uncalibrated green lightcurve and underneath the resulting time-resolved color indexes B-V_{meas} and V-R_{meas}.

6. Conclusion

The Mobile Satellite and Debris Observation System (MS-DOS) is able to reliably observe objects such as satellites and space debris. The effort required to perform such measurements is relatively low, however the preparation of the mobile system for a nightly observation is time-consuming.
From the observations, light curves can be created for the observed target. In certain cases, these light curves can be used to deduce parameters such as the rotation frequency of an orbital object. If a magnitude calibration was done the same night, the brightness of the target can be specified in apparent visible magnitudes.
However, whether parameters such as the rotation frequency can be derived from a measurement depends primarily on the observed object itself. A recurrent pattern in the light curve is the basic requirement for the successful evaluation of object-specific properties. The multispectral measurement of Cosmos-2375 contains interesting features and suggests that it is possible to derive further target properties from the multispectral analysis.
The Canon camera is the limiting factor for the observation of orbital objects in LEO due to its dead time of about one second. The applied exposure times are typically between 0.01 s and 1 s. Thus, in the best case the camera records the incoming signal in 50 percent of the observation time. For objects in MEO, the ratio of dead time to exposure time is moderate. With a typical ratio of 1/5; about 84 percent of the incoming information is recorded here.
To improve the overall system, one or both of the following options can be implemented: First, the use of a telescope with a larger aperture. Due to the larger aperture, the incoming signal intensity per pixel is greater than for the current configuration. Especially in the case of MEO objects, the measurements can be performed with a shorter exposure time which allows a more accurate evaluation of the light curve. It would also be interesting to investigate whether measurements of the Canon camera in combination with a larger telescope aperture have lower brightness fluctuations. Less fluctuation would result in a direct improvement of the multispectral analysis.
Second, the use of a camera with a smaller sensor size and less dead time. Although this reduces the maximum field of view of the system, this would not cause any differences in the light curve measurements since solely the central area of the Canon sensor is used. A lower number of pixels and a shorter dead time would improve the temporal resolution and percentage coverage, especially for targets in LEO.
Instead of a camera, the use of a continuous single photon detector would also be interesting. Although the single photon detector can not resolve the wavelength of the incoming signal for a multispectral measurement, the provided light curves have a much higher temporal resolution.

While using MS-DOS for observations, it became clear that the pointing is the limiting factor rather than the accuracy of position prediction based on TLE data. A mobile tracking system whose pointing must be recreated at the beginning of each observation night has, in the sense of pointing accuracy, no advantage over a stationary system. Despite the increasing automation of the pointing calibration, a person must be present to set up the mobile system and dismantle it again. A fixed mount allows a better starting point for fully autonomous operation, as elements such as a dome roof etc. can be controlled remotely. The process of taking measurements in OOOS has been automated so far that with few commands the connected hardware could observe orbital objects throughout the night.
Besides further improvements of the hardware, an extension of the software module LightCurveMaker2 would be favorable. A more robust algorithm for detecting objects in the captured images allows a faster evaluation of the measurements. For example, the evaluation of the object during the measurement would be conceivable. With such a function, in the process of an actual measurement the decision can be made whether the light curve of the current target contains interesting information or whether another target should be observed.
Finally, it can be said that the principle of MS-DOS can be further improved both from the hardware and the software point of view. Despite the mobility, a stationary system is better suited for observing orbital objects than the current version of MS-DOS.

References

[1] ESA's Annual Space Environment Report. ESA Space Debris Office, Apr. 27, 2017.

[2] E. G. Stansbery. "NASA's Orbital Debris Program Office, Briefing to the NASA Advisory Council". In: (Aug. 27, 2014), p. 50. URL: https://www.nasa.gov/sites/default/files/files/OrbitalDebrisProgramOffice.pdf.

[3] T. S. Kelso. CelesTrak SATCAT. URL: https://celestrak.com/satcat/boxscore.asp (visited on 06/01/2018).

[4] USA Space Debris Envirmonment, Operations and Policy Updates. National Aeronautics and Space Administration, 2011.

[5] D. J. Kessler and N. L. Johnson. "The Kessler Syndrome: Implications to Future Space Operations". In: (Feb. 2010), p. 16.

[6] IADC Space Debris Mitigation Guidelines. INTER-AGENCY SPACE DEBRIS COORDINATION COMMITTEE, Sept. 2007.

[7] K. Wormnes et al. "ESA TECHNOLOGIES FOR SPACE DEBRIS REMEDIATION". In: (Apr. 2013), p. 8.

[8] M. M. Castronuovo. "Active Space Debris Removal—A Preliminary Mission Analysis and Design". In: Acta Astronautica 69.9-10 (Nov. 2011), pp. 848–859. ISSN: 00945765. DOI: 10.1016/j.actaastro.2011.04.017. URL: http://linkinghub.elsevier.com/retrieve/pii/S0094576511001287 (visited on 05/31/2018).

[9] Space-Track.Org. URL: https://www.space-track.org/auth/login.

[10] W. Gurtner, R. Noomen, and M. Pearlman. "The International Laser Ranging Service: Current Status and Future Developments". In: Advances in Space Research 36.3 (Jan. 2005), pp. 327–332. ISSN: 02731177. DOI: 10.1016/j.asr.2004.12.012. URL: http://linkinghub.elsevier.com/retrieve/pii/S0273117704009147 (visited on 05/31/2018).

[11] T. Yanagisawa and H. Kurosaki. "Shape and Motion Estimate of LEO Debris Using Light Curves". In: Advances in Space Research 50.1 (July 2012), pp. 136–145. ISSN: 02731177. DOI: 10.1016/j.asr.2012.03.021. URL: http://linkinghub.elsevier.com/retrieve/pii/S0273117712002013 (visited on 05/31/2018).

[12] T. Endo et al. "Satellite Type Estination from Ground-Based Photometric Observation". In: (2016), p. 9.

[13] "Color Imaging Array". US3971065A. B. E. Bayer. July 20, 1976. URL: https://patents.google.com/patent/US3971065/en (visited on 06/01/2018).

[14] Bayer Filter. In: Wikipedia. Page Version ID: 842853548. May 25, 2018. URL: https://en.wikipedia.org/w/index.php?title=Bayer_filter&oldid=842853548 (visited on 06/01/2018).

[15] L. Humbert et al. "INNOVATIVE TECHNOLOGIES FOR OPTICAL GROUND STATIONS". In: 7th European Conference on Space Debris. Darmstadt, Deutschland, Apr. 2017. URL: http://elib.dlr.de/116350/ (visited on 06/01/2018).

[16] OpenStreetMap. URL: https://www.openstreetmap.org/ (visited on 05/31/2018).

[17] D. Hampf, F. Sproll, and T. Hasenohr. "OOOS: A Hardware-Independent SLR Control System". In: ILRS Technical Workshop. Oct. 2017. URL: http://elib.dlr.de/117597/.

[18] J. Alarcón-Rodrıguez, F. Martınez-Fadrique, and H. Klinkrad. "Development of a Collision Risk Assessment Tool". In: Advances in Space Research 34.5 (Jan. 2004), pp. 1120–1124. ISSN: 02731177. DOI: 10.1016/j.asr.2003.01.015. URL: http://linkinghub.elsevier.com/retrieve/pii/S0273117704000912 (visited on 06/01/2018).

[19] M. Mittag. Die Technische Performance Des Hamburger Robotischen Teleskops. Oct. 11, 2006. URL: https://www.hs.uni-hamburg.de/DE/Ins/HRT/publication/diplomarbeit.pdf.

[20] P. T. Wallace. "TPOINT — Telescope Pointing Analysis System (v4.4)". In: Starlink User Note 100 (0–1994), p. 51.

[21] K. Hirakawa and T. W. Parks. "Adaptive Homogeneity-Directed Demosaicing Algorithm". In: IEEE Transactions on Image Processing 14.3 (Mar. 2005), pp. 360–369. ISSN: 1057-7149. DOI: 10.1109/TIP.2004.838691.

[22] Angle of View - Wikipedia. URL: https://en.wikipedia.org/wiki/Angle_of_view#cite_note-1 (visited on 06/01/2018).

[23] T. W. Sudholz. "Quantifying Australian Atmospheric Properties for a Gamma-Ray Observatory to Operate at Energies Greater than 10 TeV." Thesis. 2014. URL: http://hdl.handle.net/2440/84759 (visited on 06/01/2018).

[24] M. S. Bessell, F. Castelli, and B. Plez. "Model Atmospheres Broad-Band Colors, Bolometric Corrections and Temperature Calibrations for O - M Stars". In: Astronomy and Astrophysics, v.333, p.231-250 (1998) (May 1998), p. 20.

[25] S. Kikuchi et al. "Advances in CMOS Image Sensors and Associated Processing (Part 1)". In: (Feb. 2016), p. 11. URL: http://downloads.canon.com/sensors/Canon-White-Paper-19um-High-Sensivity-CMOS-Sensor.pdf.

[26] L. Girardi et al. "Theoretical Isochrones in Several Photometric Systems: I. Johnson-Cousins-Glass, HST/WFPC2, HST/NICMOS, Washington, and ESO Imaging Survey Filter Sets". In: Astronomy & Astrophysics 391.1 (Aug. 2002), p. 204. ISSN: 0004-6361, 1432-0746. DOI: 10.1051/0004-6361:20020612. URL: http://www.aanda.org/10.1051/0004-6361:20020612 (visited on 06/01/2018).

[27] SIMBAD Astronomical Database - CDS (Strasbourg). URL: http://simbad.u-strasbg.fr/simbad/ (visited on 06/01/2018).

[28] E. Schafer. Stereoscopic Light Curve Analysis of Space Debris Objects. Dec. 3, 2017.

[29] G. Krebs. ISIS 1, 2. URL: http://space.skyrocket.de/doc_sdat/isis.htm (visited on 05/30/2018).

[30] G. Krebs. Interkosmos 24 (Aktivny-IK, AUOS-Z-AV-IK #1). URL: http://space.skyrocket.de/doc_sdat/interkosmos-24.htm (visited on 05/27/2018).

[31] D. E. C. Pearce et al. "Rapid Characterization of Geosynchronous Space Debris with 5-Color Near- IR Photometry". In: Advanced Maui Optical and Space Surveillance Technologies Conference (AMOS). 2017. URL: https://amostech.com/TechnicalPapers/2017/NROC/Pearce.pdf.

A. Appendix

A.1. Observation done with UFO

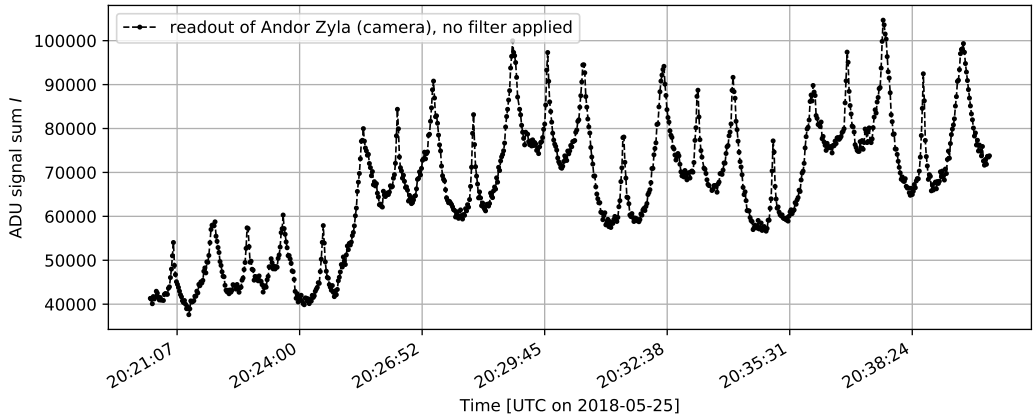

Figure A.1.: Uncalibrated lightcurve of Cosmos-2375, observed on 2018-05-25 at UFO.

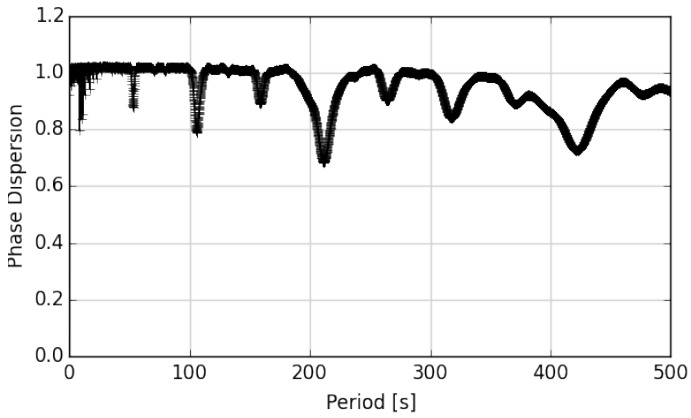

(a) Phase Dispersion Minimisation analysis

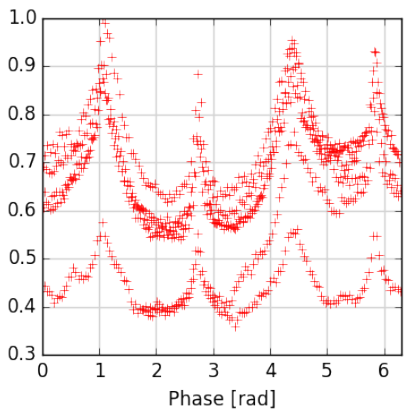

(b) PF with 211 s

Figure A.2.: PDM applied on the data set of Cosmos-2375, observed on 2018-05-25 at UFO. The most suitable period time is 211.5 s ± 7.2 s.